UNIVERSITY OF CALIFORNIA

Santa Barbara

High-Performance, Large Format Surfaces for Surface-Enhanced Raman Spectroscopy:

Increasing the Accessibility of an Analytical Platform

A dissertation submitted in partial satisfaction of the

requirements for the degree Doctor of Philosophy

in Chemistry

by

Katherine Nicole Kanipe

Committee in charge:

Professor Martin Moskovits, Co-chair

Professor Galen Stucky, Co-chair

Professor Songi Han

Professor Ram Seshadri

Professor Sumita Pennathur

March 2017

The dissertation of Katherine Nicole Kanipe is approved.

_____

Professor Songi Han

_____

Professor Ram Seshadri

_____

Professor Sumita Pennathur

_____

Professor Galen Stucky, Committee Co-chair

_____

Professor Martin Moskovits, Committee Co-chair

March 2017

High-Performance, Large Format Surfaces for Surface-Enhanced Raman Spectroscopy:

Increasing the Accessibility of an Analytical Platform

In honor of National Women's History Month 2017, for both the women who came before me and those who will come after:

"Don't let anyone rob you of your imagination, your creativity, or your curiosity. It's your place in the world; it's your life. Go on and do all you can with it, and make it the life you want to live."

-Mae Jemison, American engineer, physician, and NASA astronaut

ACKNOWLEDGEMENTS

This dissertation is dedicated to my grandmother, Helen Marie Barr

March 20, 1932 – January 26, 2015

and to my grandfather, William Edward Barr, Jr.

July 20, 1929 – June 5, 2016

If I have learned nothing else during my time at UC Santa Barbara, I have come to understand that there is no such thing as "going it alone." My life has been truly enriched by the people with whom I have surrounded myself. This, of course, includes my peers and friends all of whom have helped me to grow in unimaginable ways both as a scientist and as individual, and for that, I will always be thankful. Of particular note is my office mate, Jose Navarrete, and the other two Weird Sisters, Tracy Chuong and Katherine Mackie. My parents, Carroll and MaryEllen Kanipe, have also been supportive of me in every way, no matter how near or far from home I roam.

I am especially proud to dedicate the work presented here to my grandmother Helen (a teacher), and my grandfather Bill (a nuclear engineer), both of whom passed during my time in graduate school. My grandparents were an important part of my life, ensuring that it was always within my power to pursue my goals. Their presence is very much missed, knowing that they would be proud to see where I stand today.

I have been fortunate to collaborate with numerous researchers at UC Santa Barbara, who deserve acknowledgement here for their hard work, conversation, and inspiration. These people include Dr. Sylvia Joon Lee, Dr. Syed Mubeen, Dr. Alessia Pallaoro, Prof.

Carl Meinhart, Dr. Vicky Doan-Nguyen, Rustin Mirsafavi, each of my undergraduate students, and members of the Moskovits Group and the Stucky Group.

Undoubtedly, I have always been proud to be a graduate of UNC-Chapel Hill and now I can be equally as proud to be a graduate of UC Santa Barbara. While these schools may have been different environments in a variety of ways, both have pushed my boundaries and taught me lessons that will always be a part of the fabric of my being, as a scientist and as a citizen. I will carry the ideals of both institutions wherever I go, striving to be the best Tar Heel *and* Gaucho I can possibly be.

VITA OF KATHERINE NICOLE KANIPE
March 2017

BACKGROUND

Born in Lynchburg, Virginia (1990) and raised in Winston-Salem, North Carolina

EDUCATION

Doctor of Philosophy in Chemistry, University of California, Santa Barbara, March 2017 (expected)
      Co-advisors: Professors Martin Moskovits and Galen Stucky
      GPA: 3.96/4.00

Bachelor of Science in Chemistry, University of North Carolina, Chapel Hill, May 2012
      Undergraduate research advisor: Professor Maurice Brookhart
      Research Topic: Solid-supported Iridium Pincer Catalysts for Hydrogen Transfer
      Minor in Entrepreneurship
      GPA: 3.16/4.00

RESEARCH, MENTORING, AND TEACHING EXPERIENCE

2012-2017: Mentored ten undergraduate researchers for programs including CISEI (international summer students), AIM Photonics (community college transfer students), and CHEM 199 coursework (UCSB students)

2012-2015: Teaching Assistant, Department of Chemistry & Biochemistry, University of California, Santa Barbara

2014: Professional Development Program, two weeks of training followed by the opportunity to develop and teach a course, Institute for Science and Engineering Educators, Santa Cruz, CA

2011: Undergraduate Researcher, Center for Enabling New Technologies through Catalysis, Seattle, WA

2010: Biochemistry Intern, Advanced Liquid Logic, Research Triangle Park, NC

PUBLICATIONS, POSTERS, AND PRESENTATIONS

Properly Structured, Any Metal Can Be Plasmonic, **Katherine N. Kanipe**, Philip P.F. Chidester, Galen D. Stucky, Carl D. Meinhart, Martin Moskovits. **2017**, *manuscript in submission.*

Molybdenum Polysulfide Chalcogels as High-Capacity Anion-Redox Driven Cathode Materials for Li-Ion Batteries, Vicky V.T. Doan-Nguyen, Kota S. Subrahmanyam, Megan

M. Butala, Jeffrey A. Gerbec, Saiful M. Islam, **Katherine N. Kanipe**, Catrina E. Wilson, Mahalingam Balasubramanian, Kamila M. Wiaderek, Olaf J. Borkiewicz, Karena W. Chapman, Peter J. Chupas, Martin Moskovits, Bruce S. Dunn, Mercouri G. Kanatzidis, Ram Seshadri. *Chem. Mater.*, **2016**, 28 (22), pp 8357-8365.

A Large Format Surface-Enhanced Raman Spectroscopy Substrate Optimized for Enhancement and Uniformity, **Katherine N. Kanipe,** Philip P.F. Chidester, Galen D. Stucky, Martin Moskovits. *ACS Nano*, **2016**, 10(8), pp 7566-7571.

Nano-engineered plasmonic structures for optimized SERS performance, Poster presentation at IUPAC International Meeting, Busan, South Korea, **2015**.

Highly-Uniform Substrates for Surface-Enhanced Raman Spectroscopy, oral presentation given for Chemical Sciences Student Seminar Series, University of California, Santa Barbara, **2014**.

Emerging Frontiers in Plasmonics: Nanostructures for solar energy conversion and catalysis, Poster presentation at Materials Research Outreach Program symposium, University of California, Santa Barbara, **2013**.

Utilizing natural resources to provide sustainable access to clean water in developing countries, business plan presentation, Carolina Challenge, a university-wide entrepreneurial competition at UNC; semifinalist, **2010**.

Music for patients with hematological malignancies undergoing bone marrow biopsy: a randomized controlled study of anxiety, perceived pain, and patient satisfaction, Suzanne C. Danhauer, Tanya Vishnevsky, Cassie R. Campbell, Thomas P. McCoy, Janet A Tooze, **Katherine N. Kanipe**, Sheila A. Arrington, Elizabeth K. Holland, Mary B. Lynch, David C. Hurd, Julia Cruz. *J. Soc. Integr. Oncol.*, **2010**, 8(4), pp 140-147.

AWARDS

September 2015: Fellowship, STEM Student Support Fund, UCSB College of Letters & Science

August 2015: SciFinder Poster Award, Chemical Abstract Service & Korean Chemical Society, IUPAC Meeting

2015: MRL-DOW Travel Fellowship for attendance at the IUPAC Meeting in Korea

2014-2015: Outstanding Research Mentor Award, MRL Education Programs

2014-2015: Outstanding Teaching Assistant Award, Dept. of Chemistry & Biochemistry

2013: MRL-DOW Travel Fellowship for attendance at the MRS Fall Meeting in Boston

FIELD OF STUDY

Major Field: Materials Chemistry

Technical Skills: nanofabrication techniques including lithography, dry etching, and vacuum deposition; optical characterization techniques; electron microscopy; spectroscopy; wet laboratory techniques

Computer Skills: Microsoft Office Suite, Gimp, Inkscape, basic Python and Matplotlib programming

ABSTRACT

High-Performance, Large Format Surfaces for Surface-Enhanced Raman Spectroscopy:

Increasing the Accessibility of an Analytical Platform

by

Katherine Nicole Kanipe

Although surface-enhanced Raman spectroscopy (SERS) is a spectroscopic technique with unusually high sensitivity and molecular specificity, few practical analytical applications have been implemented that take advantage of its power. Based on what is understood about SERS from the experimental and theoretical research of the past forty years, we developed a few well-defined design principles on the basis of which a reliable and reproducibly manufacturable SERS-active substrate could be fabricated that is highly enhancing, highly uniform, stable, and based on a broad range of metals so that various chemical processes could be probed. Finally, we restricted ourselves to using only readily scalable fabrication techniques. The resulting SERS-active device was a metal over silica, two-dimensional nano-grating that was shown to produce enhancements of $\sim 10^7$ when compared to a smooth surface of the same metal. This SERS substrate also shows unprecedented signal uniformity over square centimeters, and is fabricated using commonly-available foundry-based approaches exclusively.

Initially, we explored the properties of a gold-coated substrates in which a first-order grating resonance due to long-range symmetry is augmented by a local resonance due to the individual core-shell grating elements. The SERS properties of such grating systems were systematically studied as a function of various structural parameters such as the grating pitch, the inter-element gap and the thickness of the metal layer. The most enhancing substrates were found to have a grating parameter with a radiative, rather than evanescent, first-order resonance; a sufficiently small gap between nearest neighbor grating elements to produce near-field interactions; and a gold layer whose thickness was larger than the electronic mean-free-path of the conduction electrons, so as to ensure a high conductivity for the metal layer to sustain strong surface plasmons.

We applied these same architectural principles to metals other than gold, and concluded that every workable metal (and virtually any material with sufficiently high electrical conductivity) when appropriately nanostructured, has the potential to be an efficient SERS substrate. The use of materials for SERS beyond silver and gold, has significant advantages, most importantly, allowing SERS to be used to study the surface chemistry and catalysis taking place on metals with more interesting chemistries than those of Au and Ag. Additionally, SERS substrates can be fabricated from high natural abundance, low cost materials. This was illustrated by producing SERS substrates using copper, aluminum, and nickel in addition to silver and gold which were used as benchmarks. All five metals were found to yield high SERS intensities. The variation of the SERS enhancement among them is ascribed mainly to local field effects, with the (larger) grating-based enhancement making an approximately equivalent contribution to the SERS enhancement of the five metals. This conclusion is supported by local electric field simulations.

The utility of these new grating-based SERS substrates was demonstrated by implementing them in chemical analysis in both aqueous and gas phases for which, for example, we were able to readily detect opioids such as fentanyl and morphine at concentrations as low as less than one part per billion. Additionally, we have made good progress toward integration of this substrate architecture into a microfluidic channel for a higher degree of sample workup and control.
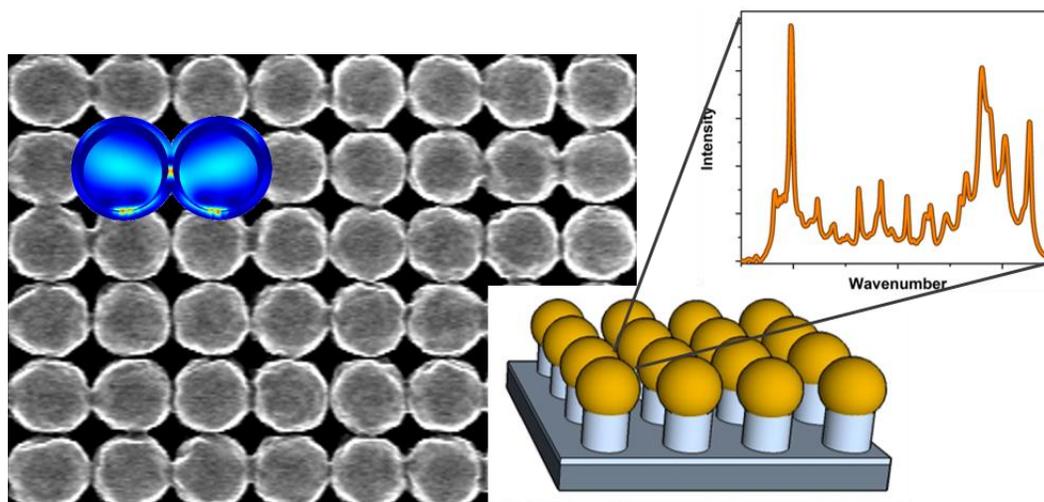
TABLE OF CONTENTS

LIST OF FIGURES

I.   An Introduction to SERS

In order to understand the work done for this project, one must have a general

understanding of surface-enhanced Raman spectroscopy (SERS). Essentially, it is a form of

vibrational spectroscopy combined with a surface effect, and an explanation of the interplay

of these two components follows.

A. *Raman Spectroscopy, a molecular understanding*

Raman Spectroscopy is a form of vibrational spectroscopy where incident light, hv, that

has been scattered by a sample is observed. When light of frequency v_0, is shone on a

sample, a very small fraction of photons are scattered. This scattered light propagates in all

directions, and while most of it retains the frequency v_0 (Rayleigh scattered light), again, a

small fraction has a different frequency, v_R, which is referred to Raman scattered light

(**Figure 1**). The frequency, v_R, is such that

$$\boldsymbol{\Delta E = h|v_0 - v_R|} \qquad \textbf{(Eq. 1)}$$

corresponds to the energy absorbed by the scatterer, [1] when $v_R < v_0$ (Stokes shifted) or

added to the scattered light when $v_R > v_0$ (Anti-Stokes shifted) though the majority of

Raman scattered photons are Stokes shifted.
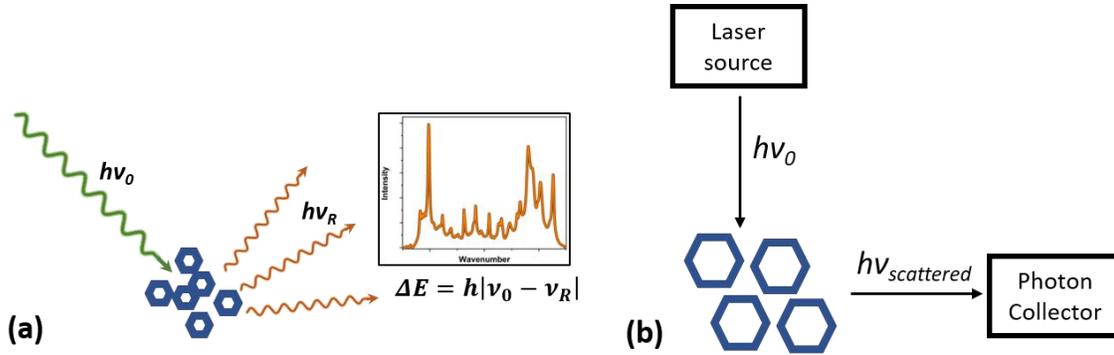
Figure 1. (a) When light of frequency ν_0 is shone on a sample, a very small fraction is scattered in all directions with a different frequency, ν_R, called Raman scattered light. This frequency ν_R, is such that $\Delta E = h|\nu_0 - \nu_R|$ corresponds to the energy absorbed by the scatterer. (b) A typical Raman scattering experiment consists of a laser source of frequency ν_0, which is directed at the scatterer, and a photon collector to collect electromagnetic radiation from the scatterer which is dispersed onto a detector.

The preceding description is purely phenomenological. To understand the process at a molecular level, one needs to consider the polarizability of a scatterer, whether that is an atom, atomic cluster, or molecule. If a scatterer is placed in an electric field (i.e. the electric field component of light), a dipole μ_{ind} is induced. The induced dipole is proportional to the strength of the electric field and is related by the constant α, called the polarizability of the scatterer.[2,3]

$$\mu_{ind} = \alpha\varepsilon \qquad \textbf{(Eq. 2)}$$

where ε is the electric field oscillating at a point in space as described by the equation

$$\varepsilon = \varepsilon_0 cos2\pi\nu \quad \textbf{(Eq. 3)}$$

The polarizability, α, is a molecular property that varies at the natural vibrational frequency of bonds within the molecule, meaning the induced dipole will radiate electromagnetic waves with frequencies ν (Rayleigh), $\nu - \nu_0$ (Stokes), and $\nu + \nu_0$ (Anti-Stokes).

2

The vibrations of a molecules can be well-described using the mathematics for a harmonic oscillator such that its total vibrational wave function may be approximated by the product of the wave functions for each normal mode of vibration. Selection rules indicate which vibrational transitions are predicted to have non-zero intensity (i.e. which transitions are allowed). These selection rules, however, do not indicate relative intensity in a Raman spectrum, and so while a frequency may be "allowed," it may be strong or weak. Simply put, the selection rules state that a transition is Raman active if the polarizability of a molecule changes during a vibration ($\Delta\alpha \neq 0$).[4]

B. Surface-Enhanced Raman Spectroscopy

Raman Spectroscopy, as has been alluded to, is a weak phenomenon. In 1974 Fleischman *et. al.* observed that for pyridine on a roughened silver surface, the Raman spectrum was unusually intense.[5] This enhanced intensity was originally attributed to an increase in the surface area of the roughened silver relative to a flat surface. The increase in intensity, however, was significantly greater than the increase in surface area as was noted by Van Duyne and Creighton in 1977.[6,7] A series of predictions[8] and calculations[9] which identified electromagnetic resonances between interacting colloidal particles as being responsible for the large enhancements and the implications this has for spectroscopy. Within a few years of these publications, the literature for surface-enhanced Raman spectroscopy (SERS) proliferated to include multiple predictions and experimental demonstrations of SERS-active systems.[10–15] In the late 1990s, Kneipp *et. al.*[16] and Nie *et. al.*[17] showed single-molecule detection by SERS under appropriate conditions, re-energizing the SERS literature with the introduction of higher-level computations and more advanced techniques for nanofabrication and nanostructure design.

C. Electromagnetic Theory of SERS

SERS occurs in the presence of nanostructured metallic features; while SERS from a single isolated metal nanoparticle has been reported, it is much weaker than that which comes from ensembles of particles. Nevertheless, it is helpful to consider just a single metal particle to start.

In the presence of a time-varying electric field as from light, oscillating surface plasmon multipoles will be sustained on a small isolated metal sphere. A surface plasmon can be described, in short, as a collective oscillation of conduction electrons against a fixed background of atom cores[18] (**Figure 2**). For particles smaller than the wavelength of incident light, only the dipolar plasmon needs to be considered, though of course, light can give rise to a variety of other excitations such as interband transitions.[19] Systems with free electrons will sustain these dipolar excitations; and the freer the electrons, the sharper and more intense the excitations.[20] When the electric field is resonant with the dipolar plasmon of a particle, the particle will emit dipolar radiation,[21] a coherent process characterized by a spatial distribution of field magnitudes around the particle. When the steady-state distribution is reached (usually within a few femtoseconds of illumination), the electric field in certain areas around the particle is depleted while in other regions it becomes concentrated.[19] Molecules subjected to the greatly concentrated fields can produce Raman spectra enhanced by several orders of magnitude over traditional Raman spectroscopy. This is the simplest explanation of SERS.

This so-called electromagnetic model of SERS was developed by Gersten, Nitzan, McCall, and Kerker[22–24] and is graphically illustrated by Käll and coworkers.[25]
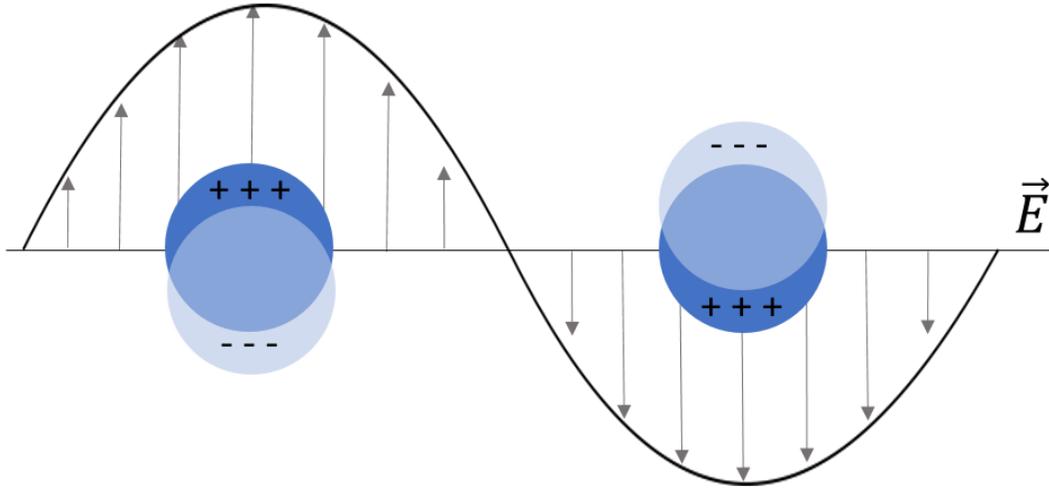
Figure 2. A surface plasmon can be described as a collective oscillation of conduction electrons against a fixed background of atom cores in the presence of a time-varying electric field as from light, illustrated here for a spherical metallic nanoparticle whose dimensions are smaller than the wavelength of light.

Even though the surface-enhanced Raman scattering is a linear optic effect (i.e. the radiated Raman field scales linearly with the incident field), the observed enhancements can represent several orders of magnitude. An understanding of how this comes to be is summarized in the following discussion.[18] Consider a spherical particle whose field enhancement averaged over its surface is g. The average magnitude of the field radiated by the particle, E_s, is then:

$$E_s = gE_0 \qquad \textbf{(Eq. 4)}$$

where E_0 is the magnitude of the incident field. A molecule at the surface of the spherical particle will experience the enhanced field E_s, and Raman-scattered light from the molecule will have field strength $E_R \propto \alpha_R E_s$ where α_R represents the Raman tensor (usually an effective tensor that more precisely characterizes the Raman scatterer as the combination of the adsorbed molecule and the surface onto which it is adsorbed[26]).

5

Not only the incident field but also the Raman-scattered field is enhanced by the spherical particle. Raman-scattered light is enhanced by a factor g', annotated with a "prime" since the enhancement may be slightly different at the Raman-shifted wavelength. At low wavenumbers, g and g' are approximately equal. The SERS-scattered field will then be

$$E_{SERS} \propto \alpha_R g g' E_0 \qquad \text{(Eq. 5)}$$

with the average SERS intensity being the square modulus of E_{SERS}:

$$I_{SERS} \propto |\alpha_R|^2 |g g'|^2 I_0 \qquad \text{(Eq. 6)}$$

As previously stated, $g \approx g'$ reducing the above proportionality to $|E_{SERS}|^2 \propto |g|^4$, meaning that the SERS intensity is enhanced by a factor proportional to the enhancement of the local incident field raised to the fourth power. The SERS enhancement should then be defined as G, the ratio of the Raman-scattered intensity in the presence of the spherical particle to the intensity in the absence of the particle:

$$G = \left| \frac{\alpha_R}{\alpha_{R_0}} \right|^2 |g g'|^2 \qquad \text{(Eq. 7)}$$

Since two forms of scattering are discussed here, it is important to distinguish scattering due to the metallic nanoparticle—which is the major contributor to SERS enhancement—from scattering due to the molecule whose Raman spectrum is reflected in the SERS spectrum, though interactions between the molecule and particle may influence the SERS spectrum that is ultimately observed. The fourth power dependence on enhancement, g, is responsible for the extraordinary enhancements observed in SERS-active systems even though there is only a first power dependence on the incident intensity, I_0.

SERS is, interestingly, one of a few truly "nano" phenomena since the effect decreases with increasing metal particle size. With structures of the order of or larger than the incident wavelength, higher order, non-radiative multipoles are excited, reducing the enhancement effect of the dipolar resonance. At the other end, as the nanostructures become too small, the electrical conductivity of the particle decreases. Moreover, in the latter limit the problem increasingly requires a fully quantum treatment.

D. *Localized Surface Plasmons in Metal Nanoparticles*

Localized surface plasmons are non-propagating, dispersive electromagnetic waves coupled to the electron plasma of a conductor at a dielectric interface.[27] A mathematical understanding of the localized surface plasmons underlying the metallic nanoparticle's scattering activity is helpful for illustration of why SERS is only efficient for particles whose dimensions are slightly smaller than the wavelength of incident light.[28] Consider a small metal sphere whose dielectric function is $\varepsilon(\lambda)$ and whose radius is R, surrounded by vacuum. The polarizability of this sphere would be given by:

$$\alpha = R^3 \frac{\varepsilon-1}{\varepsilon+2} \qquad \text{(Eq. 8)}$$

When this is combined with the expression for the dielectric function of a Drude metal modified for interband transitions:

$$\varepsilon = \varepsilon_b + 1 - \frac{\omega_p^2}{\omega^2 + i\omega\gamma} \qquad \text{(Eq. 9)}$$

where ε_b represents the contributions of interband transitions, ω_p is the plasmon resonance which is dependent on the electron density in the metal, and γ is the electronic-scattering rate. By substitution, the polarizability becomes:

$$\alpha = \frac{R^3(\varepsilon_b\omega^2 - \omega_p^2) + i\omega\gamma\varepsilon_b}{[(\varepsilon_b+3)\omega^2 - \omega_p^2] + i\omega\gamma(\varepsilon_b+3)} \qquad \textbf{(Eq. 10)}$$

The real and imaginary components of α have a pole when

$$\omega = \omega_R = \frac{\omega_p}{\sqrt{\varepsilon_b+3}} \qquad \textbf{(Eq. 11)}$$

and the width of the resonance will be $\gamma(\varepsilon_b + 3)$. The quality of the resonance is diminished when the electronic-scattering rate, γ, is large, indicating either poor conductivity of the metal or nanofeatures small enough for electronic scattering at the surface to be the dominant scattering process. SERS enhancement will diminish with the quality of the resonance. The interband transitions, ε_b, can also diminish SERS enhancement by causing an increase in the width of the resonance or a shift in the location of the dipolar plasmon resonance.[19]

E. SERS-Active Systems: Assemblies of Particles

All considerations thus far have been for a single isolated spherical particle. For SERS to be truly effective, however, assemblies of particles are needed. When individual particles are brought very close together, for example as in nanoparticle aggregates, multipolar coupling adds to the enhancement as well as dipolar coupling. The enhanced SERS intensity for two or more nanoparticles was explored in the 1980s by Metiu and coworkers[9,29] and by Gersten and Nitzan [22,30]. When the incident light is of appropriate wavelength and polarization and the gap between two particles is sufficiently small, enhancements on the order of 10^{10} are possible for molecules localized in that gap region. Käll and coworkers repeated these types of calculations to show the formation of "hot spots" (**Figure 3**) in the interstitial regions that can reach ~10^{11} or more when the particles are within 1 nm of one another and the electric

8

field component of incident light is polarized along the interparticle axis.[25] This exceeds the enhancements calculated for single particles, but falls off rapidly with increasing gap size and is virtually nonexistent when the light is polarized across the interparticle axis, mimicking the situation for a single isolated particle.
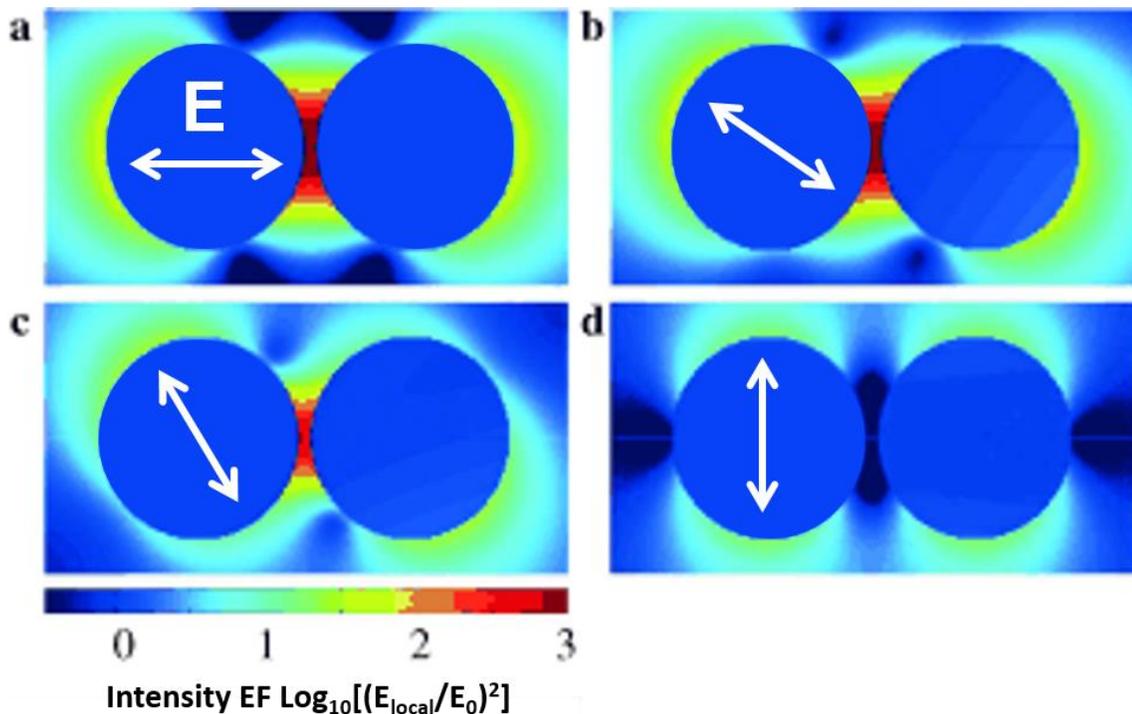
Figure 3. The formation of "hot spots" with light that is polarized along the interparticle axis (a) is illustrated here by Käll and coworkers.[25] As the polarization of the light is increasingly rotated in (b) and (c) off the interparticle axis, the intensity of the hot spot decreases until the polarization of the light is normal to the interparticle axis (d), mimicking the situation for an isolated particle in which there is no hot spot formation.

Using the above description, a list of a few essential features can be formulated for an effectively enhancing SERS-active system: nanostructured materials, materials chosen with sufficiently high conductivity (i.e. sufficiently "metallic" character), systems of interacting particles as opposed to isolated particles, and appropriate polarization of the electric field component of incident light.

II.   Large Format SERS Substrates

Herein is a report of the application of the architectural principles of grating fabrication using a square two-dimensional array of gold-coated nanostructures that achieves SERS enhancements of 10^7 uniformly over areas of square centimeters.[i] The high-performance grating substrates were fabricated using commonly available foundry-based techniques that have been chosen for their applicability to large-scale wafer processing. Additionally, we restricted ourselves to a parametric regime that optimizes SERS performance in a repeatable and reproducible manner.

A. *An Overview of SERS Substrates in the Literature*

Surface-enhanced Raman spectroscopy is a technique with unusually high sensitivity and molecular specificity, and as such efforts have been made to develop SERS-based sensors for a range of applications including the detection of analytes in biological samples,[31] explosives in military and security settings,[32] and pigment analysis in miniscule paint samples to help direct art conservation efforts.[33] All of these applications can be carried out with handheld, field compatible Raman systems.[34] The success of SERS as an analytical platform relies on the availability of highly-enhancing, uniform, and reproducible SERS substrates from which spectra are collected. A variety of approaches have been proposed to achieve high enhancement factors and a high density of so-called hot spots.[35] A rich history of using bottom-up techniques to produce, for example, highly-enhancing nanoparticles and nanoparticle assemblies is reported in the literature.[16,36,37] More recently

---

[i] Adapted with permission from Kanipe, K. N., Chidester, P. P. F., Stucky, G. D. & Moskovits, M. Large Format Surface-Enhanced Raman Spectroscopy Substrate Optimized for Enhancement and Uniformity. *ACS Nano* **10,** 7566–7571 (2016). Copyright 2016 American Chemical Society.

with advancements in nanofabrication technologies, top-down approaches have been developed, which create reproducible and inform substrate but usually with enhancement factors considerably lower than those achieved using bottom-up approaches.[38–41]

Although two dimensional gratings have been proposed for fabricating as SERS substrates since the early days of SERS,[18] few have exploited gratings as a SERS substrate fabrication strategy largely because, until recently, gratings with the requisite nanostructures could only be achieved using costly and substrate size restricted foundry technologies such as electron beam lithography.[42] Nowadays, gratings can be written on large format wafers using commonly-employed nanotechnologies such as interference or deep UV lithographies, enabling the fabrication of low cost, highly uniform and highly enhancing SERS substrates, a high performing example of which is described herein.

B. Plasmonic Gratings: Long-Range Resonance

A helpful way to understand the manner in which the grating's structure contributes to the SERS enhancement is to separate the contribution of the local field, that depends critically on the gap between neighboring elements of the grating, from far-field interactions resulting from the coherent superposition of light scattered by the grating's periodic array of elements. If the gap is large compared to the wavelength (as would be the case for, say, a two-dimensional array of well-spaced particles) one need only consider the superposition of dipolar fields. The strength of the dipolar interactions for such gratings and a number of other of its properties is found to increase dramatically for grating pitches (i.e. repeat length) above a critical value at which one of its grating orders transitions from evanescent to radiative.[43,44] The plasmonic properties of such gratings have been studied by Crozier and members of his group.[45] When illuminated by laser light resonant with one of its orders

11

above the aforementioned critical order, such a grating consisting of, for example, a two-dimensional periodic arrangement of silver or gold nanoparticles covered with an adsorbate, produce SERS spectra significantly more intense than what an equivalent number of such nanoparticles randomly arranged in solution or spaced sufficiently far apart, would.

If, however, the gap between neighboring elements is small compared to the wavelength of the light illuminating the grating, then the theory of its operation must include the effect of the near field in the vicinity of its features, or equivalently, the sum of many multipolar fields. Two-dimensional gratings in which the individual components are very closely spaced possess the added benefit of the near-field interactions, much as one achieves by bringing two nanoparticles covered in adsorbate together so as to form a small interstice—a so called SERS hot spot.[46] This effect was demonstrated for a one-dimensional grating whose SERS enhancement, however, was strongly dependent on the polarization of the excitation laser with respect to the orientation of the grating's lines.[47] The near-field interactions also drive the grating's resonances to longer wavelengths, making possible SERS excitation by commonly available lasers emitting in the red.

C. *Wafer-scale fabrication of Metallic Nano-gratings*

Fabrication Details

Substrates were fabricated using readily scalable foundry techniques such that several hundred or thousands of substrates can be made simultaneous upon a large silicon wafer and then diced and packaged or incorporated into a larger device for implementation. Here, fabrication is carried out on pre-diced square pieces (10 x 10mm or 15 x 15mm) of silicon to facilitate exploration of the parameter space for the studies discussed here. Briefly, substrates are produced from a square, two-dimensional grating fabricated by laser

12

interference lithography. Dry reactive ion etching is used to achieve pattern transfer into the

silicon, first by using an oxygen etch to break through an anti-reflection coating applied

prior to lithography and then a modified Bosch process to yield a square array of silicon

pillars. The structure is then coated with silica via plasma-enhanced vapor deposition to

produce more closely-spaced features followed by metal deposited by electron-beam

evaporation to render the structure sufficiently metallic to sustain surface plasmons. The

process flow is illustrated in **Figure 4** for clarity.
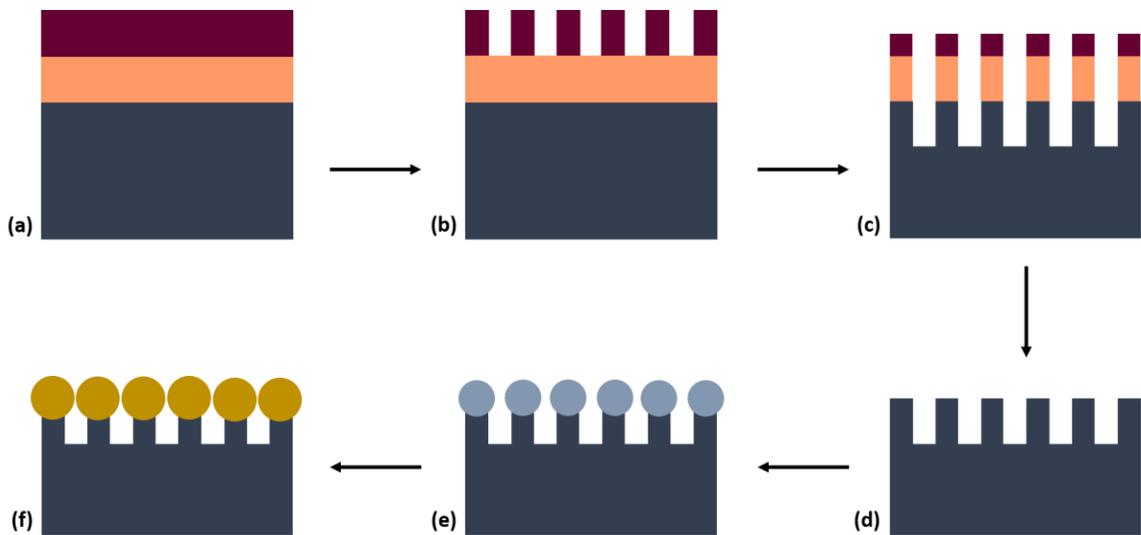
Figure 4. The process flow for substrate fabrication can be summarized as follows: (a) bare silicon is coated with an anti-reflection coating and i-line photoresist; (b) laser interference lithography is used to form two grating patterns in the photoresist at a 90° angle to one another, resulting in a square array of posts after post-exposure processing; (c) the two-dimensional grating pattern is transferred through the anti-reflection coating and into the underlying silicon using reactive ion etching; (d) upon removal of any residual anti-reflection coating and photoresist, a square array of silicon posts remains; (e) neighboring silicon posts are brought in closer proximity via deposition of silica by plasma-enhanced chemical vapor deposition; (f) the entire structure is coated with a thin film of metal by electron-beam evaporation.

Grating patterns with nanoscale periodicity can be produced using a technique called

laser interference lithography (LIL). This is a maskless lithography technique in which a

standing wave pattern is produced by the intersection of two coherent laser beams. A photosensitive layer is exposed to this standing wave pattern, a Bragg grating pattern, yielding highly regular grating lines over the entire area of beam intersection. The most straightforward way to set up such an exposure requires a s-polarized laser with a long coherent beam, a lens and pinhole, and a mirror in what is called a Lloyd mirror interferometer (**Figure 5**). A chuck holds the sample with photoresist perpendicular to the mirror and is rotatable to adjust the period of the grating. The lens and pinhole produce a diverging beam which is then aligned with the intersection of the mirror and sample. The period, *d*, of the pattern produced is governed by the equation

$$\lambda = 2d sin\theta \qquad \textbf{(Eq. 12)}$$

where λ is the wavelength of the laser source and θ is the angle defined in **Figure 5b**. This entire setup is on a vibrationally-isolated table to minimize any disturbances in the pattern caused by optical path differences of the two portions of the beam.
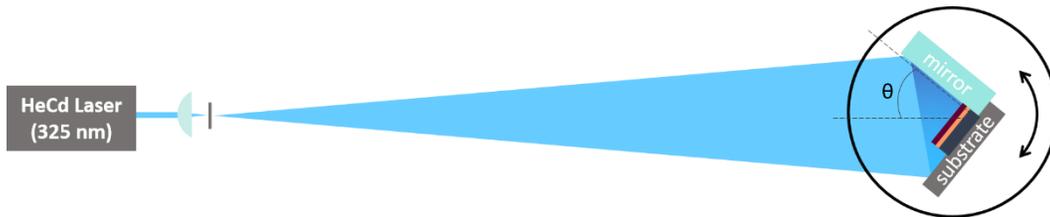
Figure 5. Schematic of a laser interference lithography setup to produce grating patterns in photoresist. This is a maskless lithographic technique in which a laser beam is spread and then appropriately combined using a Lloyd mirror interferometer to create a standing wave pattern whose period, d, can be tuned according to Equation 12. For the setup employed for this work, a 325 nm HeCd laser was used.

The primary pattern is a product of interference of the direct beam and the beam reflected from the mirror A second pattern can be caused by surface reflection and will result in standing waves in the vertical direction and is particularly problematic for highly

reflective surfaces like silicon. The addition of an extra layer between the silicon surface and the photoresist, called an anti-reflection coating, can alleviate this vertical standing wave either by absorption or by phase-shifting the reflected wave by π, or some combination of both. More complex patterns can be produced by doing multiple exposures to the interference pattern. Of interest here are dot patterns that can be produced from two exposures done at an angle to one another.

Using our specific Lloyd mirror setup, we implemented the following procedure. Silicon diced into square pieces is cleaned by sonication for 3 minutes in acetone, 3 minutes in methanol, and 3 minutes in deionized water then baked dry at 115°C for 10 minutes. The silicon was spin-coated with an anti-reflection coating (ARC, XHRiC-11, Brewer Science, Inc.). baked dry, then spin-coated with a positive i-line photoresist (PR, THMR-iP3600-HP, Ohka America, Inc.). The photoresist was soft-baked then exposed with a 55mJ dose from a 325 nm HeCd laser in a Lloyd mirror configuration ($\theta = 30$) twice with exposures made at a 90-degree angle to one another. A post-exposure bake drove off any residual solvent, then the pattern is developed (AZ300MiF, Clariant) and subjected very briefly to an oxygen plasma to clean up the final photoresist pattern. A square two-dimensional array of 120 nm diameter photoresist posts remains on the ARC-coated silicon surface with a pitch of 330 nm in both the x and y directions.

Pattern transfer can be achieved by a variety of approaches including dry and wet etching techniques. Here we use only dry etch methods due to ease of implementation, increased personal safety during processing, and the ability to do anisotropic etching. Reactive ion etching (RIE, PlasmaTherm) is a form of dry etching commonly used in microfabrication in which a chemically reactive plasma is initiated by applying a strong RF

15

electromagnetic field across two electrodes such that ions from the plasma bombard the substrate placed in between the electrodes (**Figure 6**). These ions react chemically with the materials on the surface and by-products are pumped out of the etch chamber. Material can also be removed via sputtering if the bombarding ions transfer some of their kinetic energy to the surface materials. Etch conditions are dependent on several parameters such as choice of gas, flow rates, chamber pressure, and RF power.
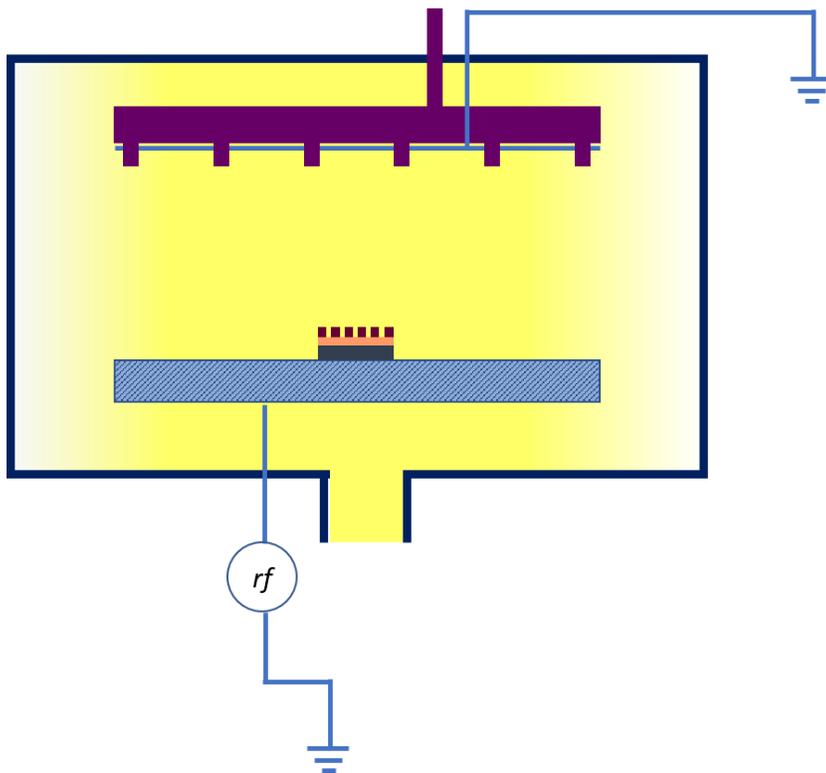
Figure 6. Schematic of reactive ion etching chamber. The basic setup is approximately the same for both the low-power oxygen etch needed to break through the anti-reflection coating and the modified Bosch process (simultaneous flow of SF_6, C_4F_8, and Ar_2) used to transfer the pattern into the underlying silicon.

A low-power oxygen RIE process is used to transfer the square array dot pattern from the photoresist to the anti-reflection coating so that the underlying silicon is exposed for further etching into the silicon.

A form of RIE called deep reactive ion etching (DRIE, PlasmaTherm) is used for etching into the silicon to attain a highly anisotropic etch that allows for steep-sided, high aspect ratio holes and trenches. A modified-Bosch process is used for transfer of the square two-dimensional array pattern into the silicon. Typically, a Bosch process cycles through the flow of three gases for high aspect ratio etching into silicon: SF_6 as a reactive etchant, C_4F_8 as a passivation layer, and Ar_2 to sputter away residual etched material. In the modified Bosch process, all three gases are flowed simultaneously to maintain a more consistent side wall profile and avoid the scalloped pattern common due to a traditional Bosch process.[48]

For the substrate produced here, the silicon is etched to an approximate depth of 350 nm. Etching is followed by removal of any residual lithography materials using a piranha solution (3:1 sulfuric acid and hydrogen peroxide) warmed to 35°C for at least 1 hour. Substrates are then rinsed with deionized water and blown dry using $N_{2\,(g)}$.

Since the intention is to excite both long range resonance via grating symmetry and short range resonance due to near-field effects, the individual grating elements (i.e. individual silicon posts) must be brought in close proximity and bestowed with metallic character.

The proximity requirement is satisfied by depositing silica via plasma-enhanced chemical vapor deposition (PECVD, Advanced Vacuum) such that the post diameter is increased. Chemical vapor deposition is a technique in which gaseous species are brought in the vicinity of a heated substrate surface in an activated (i.e. heat, light, plasma) environment to form thin films and coatings upon formation of stable solid species. This process can involve both gas phase reactions and heterogenous reactions at the surface of the substrate. PECVD, specifically, involves chemical reactions that happen after generation of a plasma of the reactive gases using RF frequency discharge between two electrodes (**Figure**

17

7). Silica is deposited onto these substrates by flowing SiH_4, He, and N_2O at 300°C. PECVD does not result in conformal coatings of substrates, rather the formation of a spherical silica cap is observed on top of posts in the silicon array.
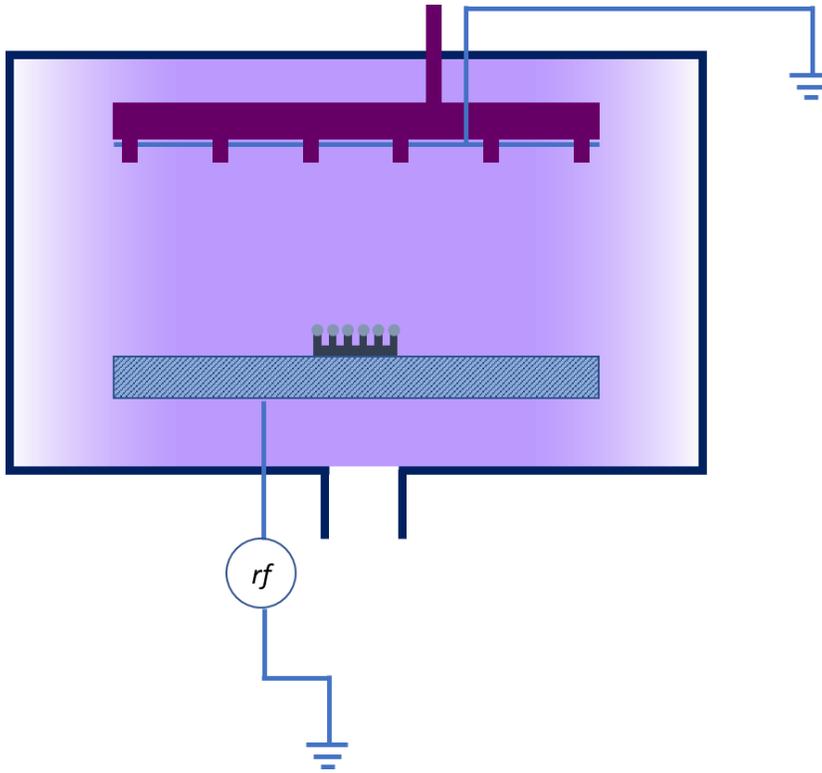
Figure 7. Schematic of plasma-enhanced chemical vapor deposition chamber. A flow of SiH_4, He, and N_2O at 300°C is used to generate a plasma from which silica can be deposited onto the silicon structure.

The final step in substrate processing is the deposition of metal by electron-beam evaporation (EB, Temescal). EB evaporation is a physical vapor deposition technique done under high vacuum ($<10^{-6}$ Torr) in which a beam of electrons are generated from a filament underneath a source material and redirected via electric and magnetic fields to strike the source (**Figure 8**). The source is heated in this way until it starts to evaporate, then atoms condense onto everything within line of sight in the evaporation chamber, forming a thin film of the source material. EB evaporation is a highly anisotropic deposition technique, and

so the resulting metallic layer deposited onto substrates can best be described as

hemispherical or cross-sectionally, crescent shaped.
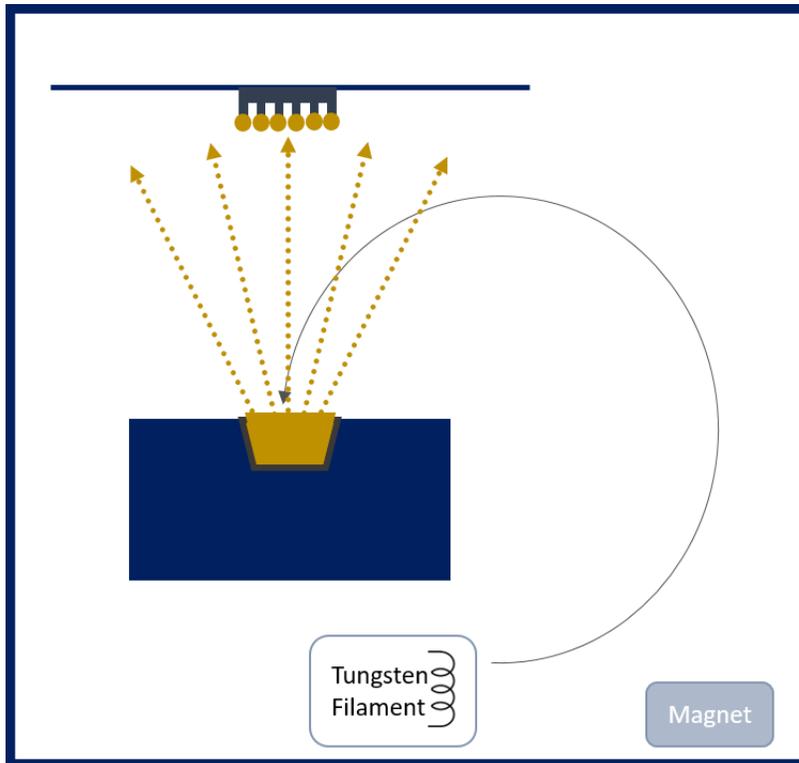
Figure 8. Schematic of electron-beam evaporation chamber. A beam of electrons is generated by energizing a tungsten filament; the electrons are then directed by magnet toward a source material, which is heated to evaporation. Evaporated material is deposited in a line of sight fashion on the substrate, positioned above the source material.

Topographical Analysis

The topography of the substrates was studied using scanning electron microscopy

(SEM). SEM images of intermediate steps as well as the final product were collected to fully

elucidate the substrate structure and are shown in **Figure 9**. Panels (a) and (d) show the

underlying silicon structure after etching and liftoff in piranha solution. The periodicity is

measured to be 330 nm with individual structures being pillars of diameter 120 nm and

height 350 nm. The two-dimensional grating pattern is retained over the entire piece of silicon apart from the edges, where defects in the lithography are common, particularly for square substrate. These edge areas are excluded from further analysis. The silica cap resulting from PECVD is shown in panels (b) and (e) and has a diameter of 270 nm as measured in the *xy*-plane parallel to the substrate surface. The non-conformal nature of the silica film is apparent in the spherical nature of the cap, though silica can also be found in the interstitial spaces between the bases of neighboring pillars. Silica thickness is reported in all subsequent text as a mass thickness (i.e. the thickness of silica deposited onto a flat, polished silicon surface under identical deposition conditions). The thickness deposited directly on top of the silicon pillars is approximately equal to the mass thickness.
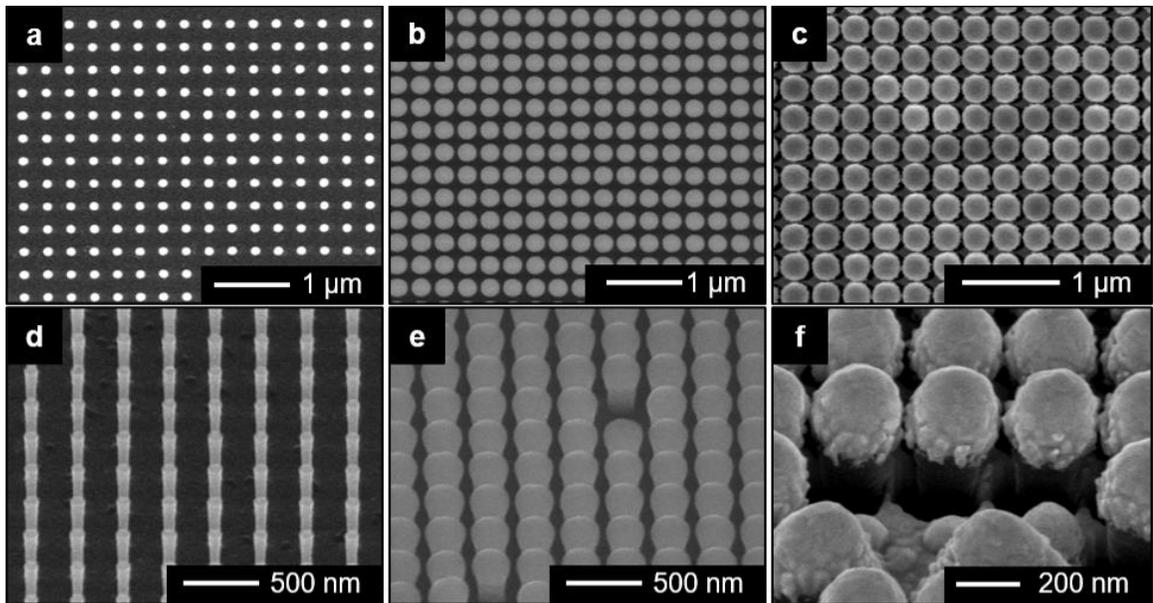
Figure 9. Scanning electron micrographs elucidating the results of the fabrication processs: (a,d) lithography and etching; (b,e) plasma-enhanced chemical vapor deposition of silica; (c,f) and electron-beam evaporation of gold. The periodic nature of the structures in both the *x* and *y* directions, and the modulation of the structures' dimensions *via* silica deposition are clearly apparent. Images a, b, and c are top views and images d, e, and f are taken at a 45° tilt to show the profile of the structures. (The images shown in e and f were chosen purposely to because they show rarely-encountered defects that illustrate the under-structure of the Si/SiO$_2$/Au core-shell grating elements.)

Panels (c) and (f) show the final structure of the substrate after the completion of EB evaporation. Metal is shown to be deposited as a hemispherical cap on the silica/silicon grating elements. It may be noted that the roughness of the metal-coated surfaces is greater than that of surfaces only coated with silica. This is because EB evaporation is a physical vapor deposition method as opposed to a chemical one, and as such, is more prone to the deposition of small clusters rather than single atoms of material. Again, this thickness of metal coatings is reported as a mass thickness, which refers to the thickness of material deposited as recorded by a quartz crystal monitor and is approximately equal to the thickness of metal directly on top of the entire structure.

D. SERS Performance and Uniformity Analysis

Substrates were fabricated as described above, using gold as the metal coating deposited by EB evaporation. An analysis of the substrate's SERS performance over large areas follows as well as a description of the optimization process to maximize the observed SERS intensities.

SERS measurements were carried out using a Horiba Raman microscope equipped with a 633 nm laser on substrates onto which thionine was allowed to adsorb for 18 to 24 hours in a micromolar aqueous thionine solution, ensuring at least monolayer coverage. The thionine molecule forms a sulfur-Au bond with the gold substrate surfaces and produces a well-defined SERS signal due to its large Raman scattering cross-section.[49] The spectra obtained are in good agreement with literature spectra. Additional, a broad luminescence background was observed, a common feature of SERS, which was subtracted from the overall spectra so as to compare true SERS intensities when computing enhancement.

The highest observed intensity 4.3 x 10^7 counts per milliwatt per second for the major

thionine peak near 487cm^{-1} when the substrate was exposed for 0.25 seconds with an

incident laser power of 7.6 µW.

A single crystal gold surface dosed with thionine in the same manner produced a SERS

signal of 7.4 counts per milliwatt per second using the same illumination conditions,

corresponding to an enhancement of ~10^7 (**Figure 10a**). The enhancement was calculated in

accordance with the expression presented by Le Ru and Etchegoin, where

$$EF = \frac{I_{SERS}/N_{surf}}{I_{RS}/N_{vol}} \qquad \textbf{(Eq. 13)}$$

which is commonly used to compare average SERS enhancements across different

surface.[50] The SERS substrates are assumed to have surface areas that are approximately

equal to that of a planar single crystal gold surface, eliminating the need to estimate the

number of molecules active in the SERS measurement – a common source of error in

computing SERS enhancements, as well as issues of variable quenching of molecular
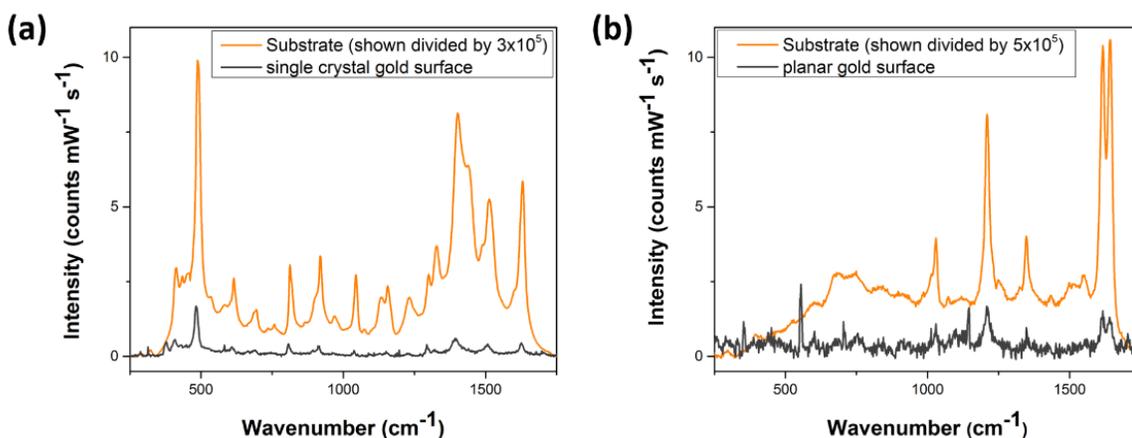
resonances on the two samples.

Figure 10. (a) The enhancement was determined by comparing the SERS intensity recorded for thionine adsorbed onto the grating substrate to the intensity measured

from adsorbate-covered single crystal gold. The plotted intensity from the substrate is shown divided by a factor of 3x10^5 for clarity relative to the scale of the single crystal gold. (b) The SERS spectra of 1,2-bis-(4-pyridyl) ethylene adsorbed on a gold SERS substrate and on a planar gold surface confirms the enhancement determined using thionine. The planar gold surface is a 100 nm-thick layer of gold deposited by electron-beam evaporation.

The enhancement of the substrate was also measured using millimolar solutions of 1,2-bis-(4-pyridyl) ethylene (BPE). This molecule yielded enhancements ~10^7 as well (**Figure 10b**). BPE was chosen because it bonds to gold substantially more weakly than thionine does, and unlike thionine, BPE is not resonant with the 633 nm wavelength of the exciting laser, thereby eliminating the likelihood that the large SERS enhancement observed for thionine resulted from the (unlikely) possibility that it binds differently to non-crystalline gold than to single-crystal gold, thereby creating new channels for chemical enhancement.

The substrate design was optimized by exploring the available geometric parameters space that makes use of key principles relevant to gratings and plasmon excitation: a grating order that is radiative rather than evanescent; nanogaps that sufficiently small to produce hot-spots; and a gold coating that is sufficiently thick (i.e. sufficiently metallic) to support sharp surface plasmons. These design parameters were controlled by varying the grating pitch, silica thickness, and gold thickness. The approach is performance driven, meaning that the substrates were optimized for use with a 633 nm laser. Accordingly, an exhaustive examination of the resonance dependence due to parameter manipulation was not the goal. Aspects of such wavelength tunability in grating structures were investigated previously by groups such as Crozier, *et. al.*,[45] and the results of these studies can be applied to tune the substrate design to a different laser source.

The grating pitch (i.e. repeat length) was varied between 240 and 330 nm, which represents the full range of grating pitches achievable with the available LIL instrumentation. The transition between evanescent and radiative grating orders becomes apparent in the observed SERS intensities (**Figure 11a**). Furthermore, spectroscopic ellipsometry was used to obtain the reflectance spectrum at normal incidence $R_0(\lambda)$ from which the normal incidence absorbance spectrum $A_0(\lambda)$ was calculated. An absorbance feature associated with the first order grating resonance is clearly visible for gratings with appropriate grating parameters, as is the transition from evanescent to radiative modes (**Figure 11b**), which is signaled by a change both in peak position and quality favor of the absorption band with changing grating pitch. As expected, the absorbance feature for the most enhanced gratings showed a maximum near the wavelength of the excitation laser (633 nm).
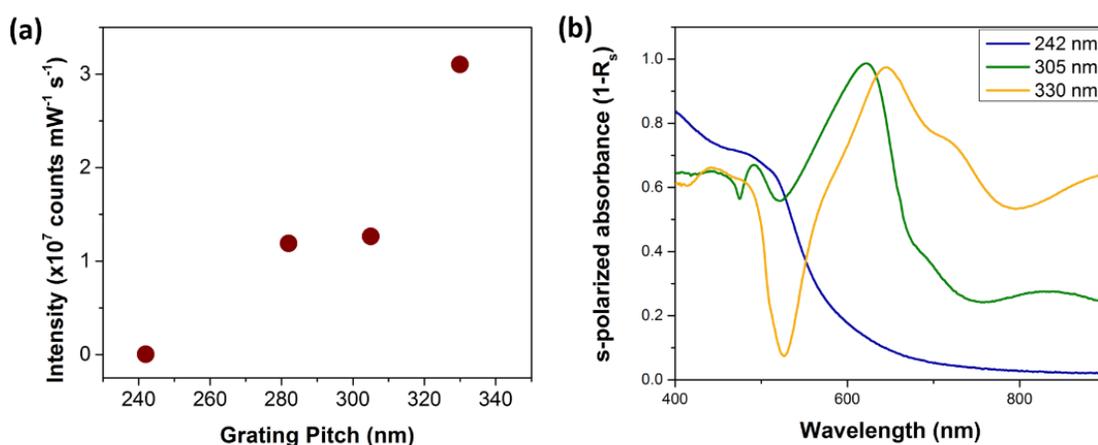
Figure 11. (a) Measured SERS intensity versus grating pitch; samples shown have pitches of 242 nm, 282 nm, 305 nm, and 330 nm; gap size and gold thickness are held approximately constant at 16 nm and 105 nm, respectively; (b) absorbance (one minus normal reflectance) versus wavelength; the transition from an evanescent grating order to a radiative one is apparent with increasing grating pitch; samples with pitches of 242 nm, 305 nm, and 330 nm are shown here; the sample with a pitch of 282 nm is excluded for clarity.

Briefly, spectroscopic ellipsometry (SE, Woollam variable-angle spectroscopic ellipsometer), is an optical characterization technique in which the change in polarization of light reflected or transmitted from a material structure is measured as an amplitude ratio, Ψ, and phase difference, Δ. The measured response is dependent upon the material's optical properties and thickness, so SE is often used to measure the thickness and dielectric of thin films.

The gratings produced were considered to be effective optical media since their features are smaller than the wavelength used to excite surface-enhanced Raman (633 nm). One can then assume that the media can be described by effective optical constants (n, k). Because the structure of the gratings is somewhat different in the directions normal and tangential to the plane of the grating, in general, one would have to use Fresnel coefficients that related to a uniaxial anisotropic medium and also the fact that the grating might be construed to be a film on top of a silicon substrate. However, the grating is sufficiently thick that no light penetrates to the silicon substrate. Accordingly, it is assumed the ellipsometric measurements were carried out on a single, infinite medium. We also ignored its anisotropy for two reasons: first, we noted that the values of n and k returned by analysis of the Ellipsometric values at various angles of incidence did not vary a great deal, and second, we used the optical constants returned by the calculation to compute normal incidence reflectance value which depend only on the tangential optical constants, independent of the angle of incidence.

The two quantities Ψ and Δ are related to the complex-valued Fresnel coefficients $\hat{r}_{s,p}$ follows.[51] (The caret indicates complex values.)

25

$$\frac{\hat{r}_p}{\hat{r}_s} = \rho = \tan\Psi e^{i\Delta} \qquad \text{(Eq. 14)}$$

The optical constants, n and k, of an optically isotropic surface measured at angle of incidence θ, can be calculated from the ellipsometric parameters using the following expression:[52]

$$(n + ik)^2 = \sin^2\theta \left[1 + \tan^2\theta \left(\frac{1-\rho}{1+\rho}\right)^2\right] \qquad \text{(Eq. 15)}$$

The s-polarized reflectance, R_s, was calculated using the expression $R_s = \hat{r}_s^* \hat{r}_s$ in which the asterisk denotes the complex conjugate, and $\hat{r}_s$ is the s-polarized Fresnel function:

$$\hat{r}_s = \frac{\hat{n}_i \cos\theta - \hat{n}_t \cos\varphi}{\hat{n}_i \cos\theta + \hat{n}_t \cos\varphi} \qquad \text{(Eq. 16)}$$

in which $\hat{n}_t = n + ik$ as defined above, $\hat{n}_i$ is the complex refractive index of the incident medium (approximately equal to 1 if the medium is air), and φ is the complex angle of refraction in the effective medium that can be calculated from the value of θ using Snell's law. For normal incidence both θ and φ are zero, and the reflectance is given by:

$$\hat{r}_o = \frac{\hat{n}_i - \hat{n}_t}{\hat{n}_i + \hat{n}_t} \qquad \text{(Eq. 17)}$$

The fraction of the incident light energy reflected is $R_o = \hat{r}_o^* \hat{r}_o$, which will be a function of the wavelength. Therefore, the fraction of the incident energy absorbed will be

$$A_o(\lambda) = 1 - R_o(\lambda) \qquad \text{(Eq. 18)}$$

Spectra of $A_0(\lambda)$ are shown in **Figure 11b**.

The silica layer was varied to control the gap size between vicinal elements by depositing thicknesses that varied between 50 and 284 nm. Since smaller interstitial regions tend to produce more intense hot spots,[53] a study of average interstitial gap sizes between 16

nm and greater than 100nm—holding all other parameters equal—confirmed that even small

variations in the gap size resulted in noticeable changes in signal intensity (**Figure 12**). The

smallest gap size used, 16 nm, was still considerably larger than the small gaps (~1 nm)

below which quantum effects cause the SERS enhancement to *decrease* with decreasing gap

size.[54] As expected, the smallest gap size interstitial gap size resulted in the largest observed

SERS intensities.
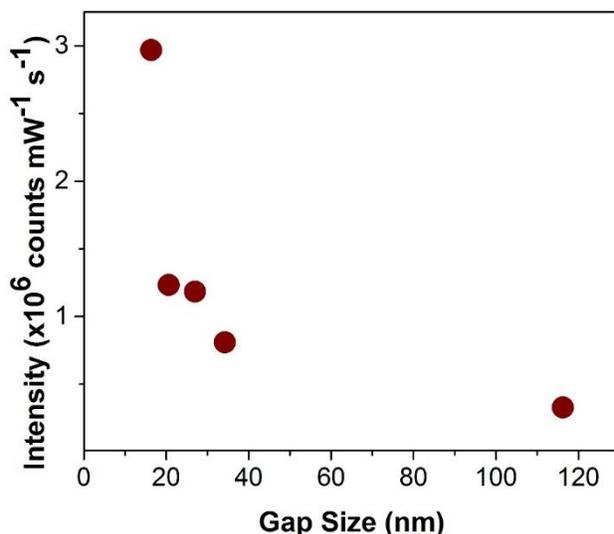
Figure 12. SERS intensity versus gap size, which drops off rapidly and results in weak SERS intensities beyond ~20 nm gap size; sample shown have gap sizes of 116 nm, 34 nm, 27 nm, 21 nm, and 16 nm; grating pitch and gold thickness were held approximately constant at 330 nm and 120 nm, respectively.

The effect of gold layer thickness was also investigated by incrementally varying the

thickness of the gold overlayer from 50 to 120 nm (**Figure 13**). Since reduced conductance

of the metal will result in less effective confinement of the optical field,[55] the thinnest gold

layer was chosen to be approximately equal to the mean free path of the conductance

electrons in gold, at and below which the metal's conductance would be reduced,

broadening the surface plasmon resonance. The SERS intensity, indeed, increased

monotonically with the thickness of the gold layer (keeping all other parameters constant, including gap size). Not unexpectedly, the SERS intensity is more sensitive to the interstitial gap size than to the gold layer thickness.
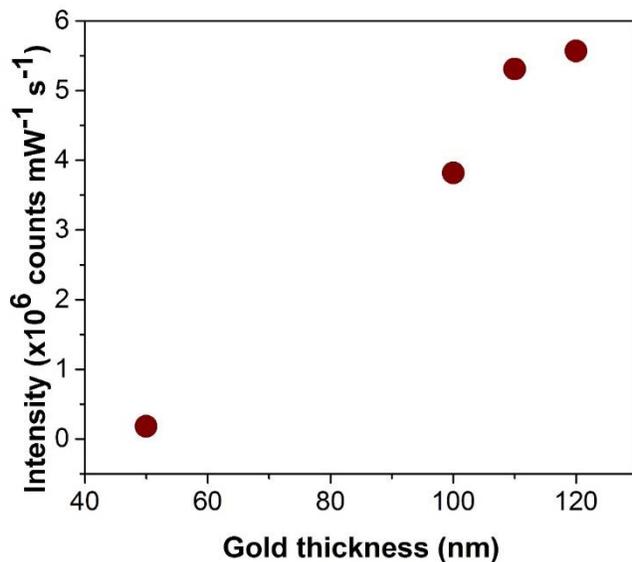
Figure 13. SERS intensity versus gold thickness; substrates with a gold layer that demonstrates poor conductance give weak SERS intensities while those with more metallic character give strong SERS intensities; samples shown have gold thicknesses of 50 nm, 100 nm, 110 nm, and 120 nm; grating pitch and gap size were held approximately constant at 330 nm and 18 nm, respectively.

Optimizing their nano-structural parameters yielded substrate with SERS enhancement $\sim10^7$ uniformly across the entire fabricated area using 633 nm excitation, when the grating pitch is greater than ~300 nm, the gap size less than 20 nm, and the gold mass thickness at least 80 nm. Smaller gap sizes (but greater than 1 nm) would produce even greater enhancements; however, such interstices would restrict the size of the molecules that could be investigated. Many proteins and other biomolecules or polymeric species would not be able to penetrate the interstices. Somewhat greater enhancements might be possible with a hexagonal rather than square grating and by continued fine tuning of the structural variables

of the grating. The improvements will be rather marginal in a regime that is close to the highest SERS enhancements reported to date uniformly over so large a substrate area. Of course, it is possible to construct individual hot spot in which very small molecules might produce greater SERS enhancements;[56,57] however, we believe what we have reported is among the highest SERS enhancements uniformly measurable across an area $>1cm^2$, using a technology that has been demonstrated in other contexts to be scalable to large wafer formats.[58]

The substrates' SERS intensity uniformity was determined by measuring the intensity distribution function obtained from a map of the SERS intensities measured over several randomly chosen 100 x 100 um portions of their surface, an example of which (mean = 7.4 x 10^6; FWHM = 3.6 x 10^6) is shown in **Figure 14**. WE find that 95% of the surface yields SERS intensities that vary by factors less than a factor of 2, so far the most uniform SERS substrate reported, and very greatly more uniform than what is obtained for substrates comprised of aggregated noble metal nanoparticles in which the SERS-active assemblies vary from monomers to large aggregates whose SERS enhancements can vary by a factor of 10^3 or more.[50]
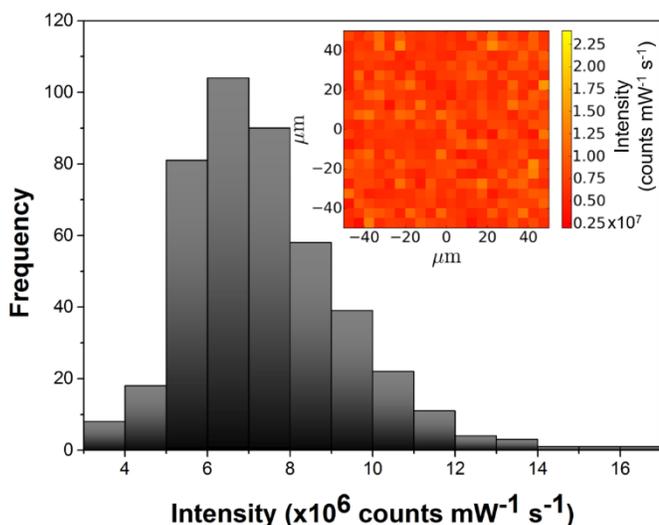
Figure 14. A typical distribution of intensities measured over a 100 µm x 100µm area of a substrate taken at 5 µm intervals in the *x* and *y* directions. The average SERS intensity is $7.4 \times 10^6 \pm 3.6 \times 10^6$ counts (0.25s exposure at 7.6 µW). The inset shows the spatial distribution of intensities over the mapped area. The area shown is from a sample fabrication with a grating pitch of 330 nm, a gap size of 17 nm, and a gold thickness of 80 nm.

III.   Properly Structured, Any Metal Can Be Plasmonic

In this chapter, we argue that virtually any material with sufficiently high electrical conductivity, appropriately nanostructures, has the potential to be an efficient SERS substrate. While silver and gold have been the dominant plasmonic metals used for SERS since the field's inception, metals with advantages such as high natural abundance, low cost, and useful catalytic activity could be used as the basis for SERS substrates. We illustrate this premise using our aforementioned fabrication scheme for creating large-format SERS substrates and five metals: silver, gold, copper, aluminum, and nickel, all of which are found to yield high SERS intensities. Their enhancement is ascribed mainly to the grating-based enhancement of the architecture with local field effects influencing only their SERS

30

performance relative to one another. This conclusion is supported by local electric field simulations.

A. Non-Traditional SERS Metals in the Literature

Silver and gold have dominated the SERS literature since the inception of the field, on account of their favorable and high quality plasmonic properties in the visible region of the spectrum and their high chemical stability. Indeed, the phenomenon was originally observed on roughened silver surfaces[6] that are still commonly used as SERS platforms in biological applications,[31,59,60] for detecting low concentration analytes,[36] and in other sensing applications.[61,62] Not unexpectedly, a great deal of interest has been focused on understanding both theoretically[63,64] and experimentally[20] what structural characteristics and materials properties lead to a highly effective SERS substrate for analytical applications.

Strategies for improving SERS performance have largely centered on optimizing the architecture of SERS substrates, for example, by developing strategies for reproducibly aggregating nanoparticles,[41] or producing such electromagnetically coupled nanostructures as nano-gratings,[45] piezoelectrically driving a nanotip towards a metal surface as in TERS,[65] and synthesizing core-shell nanoparticles, in which the plasmon of a nanocavity couples to the plasmon of a nanosphere.[66] It has been known from the earliest days of SERS that most metals can sustain plasmons, among which only the alkali metals rival the coinage metals in the plasmonic capabilities.[67] Although excellent SERS results were reported with alkali metals under ultra-high vacuum conditions,[68] their lack of stability in air and in water make the alkalis impractical for most applications. The plasmonic properties of other high conductance metals have been explored theoretically including Cu, Pt, Pd,[69,70] and early SERS results using Al, Pt, and In have been reported.[71–75] The plasmonic resonance quality

(i.e. the "sharpness" of the resonance) has been discussed by several workers.[76] It is easy to show that the breadth of the plasmon resonance of a sphere whose radius is much smaller than the wavelength, increases with increasing electron scattering rate (which is inversely proportional to electrical conductivity) and with increased interband contribution to the material's dielectric constant in the frequency range of the plasmon. (these two properties account for the good plasmonic performance of silver). Also well-known is the fact that the plasmon resonance frequency can be significantly tuned by altering the nanogeometry of the plasmonic entity; for example, one (or more) of the three degenerate plasmonic modes of a Pd nanosphere (in air) whose resonance occurs at ~230 nm can be shifted to cover the entire visible and near IR spectrum by either elongating the sphere to a prolate spheroid or flattening it to an oblate spheroid.[77]

Previously discussed was a nano-grating architecture that produces both highly enhancing and highly uniform SERS signals over wafer-scale areas.[78] The key to strong performance of this architecture, which was reported using a gold metallic layer, is the synergy of local near-field resonances resulting from interactions between neighboring grating elements and long-range grating resonance. The nature of the grating contribution has been capably discussed in the literature,[43,44] an important point being that grating resonances are, to first order, a function of the geometrical parameters of the grating, independent of the material. Here we apply such architectural principles to a variety of metals to show that the grating-enabled plasmonic resonances allow a wide range of metals to function effectively as SERS active systems.

Expanding the pool of SERS-capable metals beyond silver and gold has important implications. For example, aluminum is earth abundant and therefore inexpensive; and

nickel, copper, platinum, palladium, and many other transition metals, make possible the study of important surface chemical and catalytic processes, using SERS. Although few such attempts have appeared, and none discussing the ubiquity of plasmonic materials systematically as we do here, such goals are not altogether new. For example, Michael Weaver[79] pioneered studies in the 1980s using palladium-coated gold electrodes, motivated by the desire to use SERS for studying chemistries for which gold is not suitable.[80–82]

Here we demonstrate that by using our prescriptive two-down nanofabrication method, a silica/silica nanograting can serve as a common substrate on top of which essentially any metal can be deposited to create a highly functional SERS substrate. We illustrate this using five metals: gold, silver, copper, aluminum, and nickel. The first two—traditional SERS materials—are the benchmarks against which the performance of the others are compared. Copper was chosen to complete the set of coinage metals, and to illustrate the negative effects on enhancement of interband transitions occurring in the vicinity of the plasmon resonance. Aluminum is earth abundance and a good conductor whose dielectric function in the visible region of the spectrum is almost devoid of interband contributions. Nickel is not a particularly good conductor and has strong interband transitions in the visible; but it is a metal with rich surface chemistry.

B. SERS Substrates Fabricated with Various Metals

The two-dimensional grating pattern previously discussed was fabricated in silicon with a 330 nm pitch; silica was deposited to a mass thickness of 200 nm by PECVD; and metal was deposited to a total mass thickness of 104 nm. Silver, gold, aluminum, and nickel are deposited by EB evaporation; first a 4 nm Ti adhesive layer is deposited then a 100 nm layer of the chosen metal is deposited on top. Copper is deposited by thermal evaporation (TE) to

a thickness of 104 nm. No titanium layer is deposited for copper-coated substrates, so the thickness was chosen to match that of other metal-coated substrates such that the gap size remains consistent.

Thermal evaporation is a physical vapor deposition technique in which source material is placed in a resistive heated boat under high vacuum ($<10^{-6}$ Torr) until it evaporates toward the substrate where the material condenses onto the surface.

SEM visualization of substrates reveals that the grating architecture is effectively maintained for all choices of metal (**Figure 15**). While minor variations in surface roughness occur, most notably for nickel, the high uniformity of the two-dimensional grating arrangement of core-shell elements is apparent for all five metals over large areas as shown in **Figure 15f** for silver over several square microns.
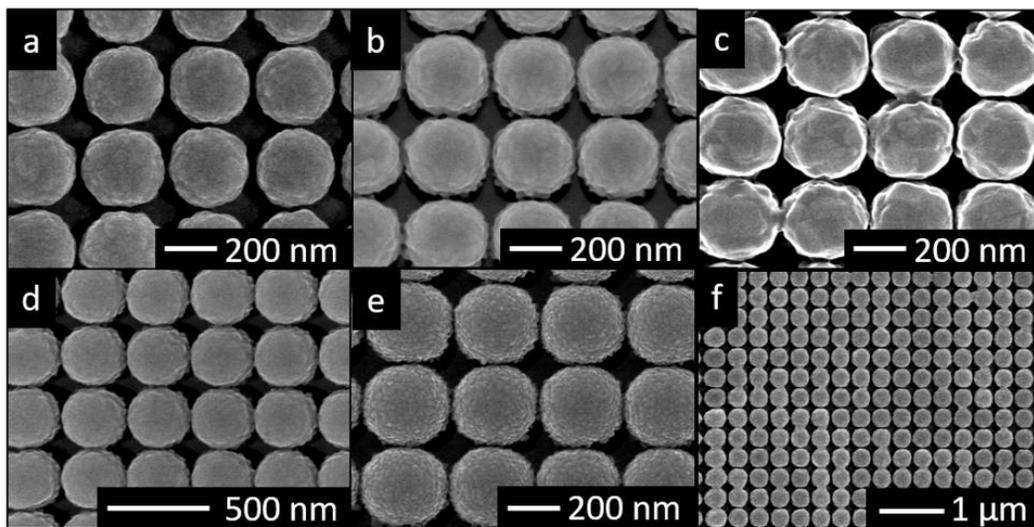

Figure 15. Scanning electron micrographs for SERS substrates fabricated with (a) silver, (b), gold, (c) aluminum, (d) copper, and (e) nickel show that repeatability of the topography previously shown with just gold. The uniformity is retained across several square microns as seen in (f).

The resonances of these systems were determined using reflectance spectroscopy (Cary 500) at normal incidence, from which the absorbance was calculated by noting that the transmittance is zero. As seen in **Figure 16**, the absorbance spectra for all of the substrates is composed of several absorbance features among which two can be assigned directly. The first, and most prominent features occurs at approximately 600 nm and corresponds to a radiative, first-order grating resonance. That this resonance overlaps the 633 nm laser used in SERS experiments is intentional since the pitch of the grating was selected explicitly to achieve this overlap,[45] thereby ensuring strong SERS enhancement. While the maximum of this resonance does not exactly overlap with 633 nm for all of the metals used, the pitch of the grating could be further fine-tuned to do so for each metal if that level of precision is desired.

The other prominent feature occurs beyond 800 nm and is representative of near-field effects. A simple effective medium calculation for the corresponding silica@metal core-shell particles suggests that these absorption peaks are resonances due to the near-field interactions between neighboring elements.
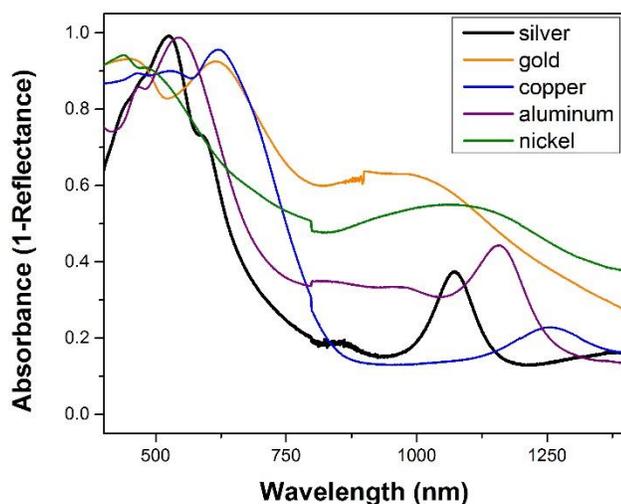
Figure 16. Absorbance (one minus Reflectance) versus wavelength as measured at normal incidence by a uv-vis-nir spectrophotometer for all five choices of metal. For substrates of each metal, two major features can be observed: a radiative first order grating resonance near 600 nm and a core-shell resonance that occurs beyond 800 nm.

SERS performance was demonstrated with thionine adsorbed to full monolayer coverage. Un-adsorbed thionine was washed away and SERS spectra collected in backscattering mode using 7.6 microwatt incident power from a 633 nm laser and 0.25 – 2.5 second exposures. All reported values for SERS intensity are converted to counts per milliwatt per second for direct comparison.

Silver and aluminum substrates were pre-treated to remove air-formed oxides by submerging the substrates in millimolar hydrochloric acid and millimolar sodium hydroxide, respectively. Silver, not unexpectedly, gives the highest SERS intensity, outperforming the previous gold substrates by a factor of 4-5. **Figure 17** shows thionine spectra as observed from each metal substrate. The measured SERS intensities (highest to lowest) were in the following order: silver, gold, copper, aluminum, nickel.
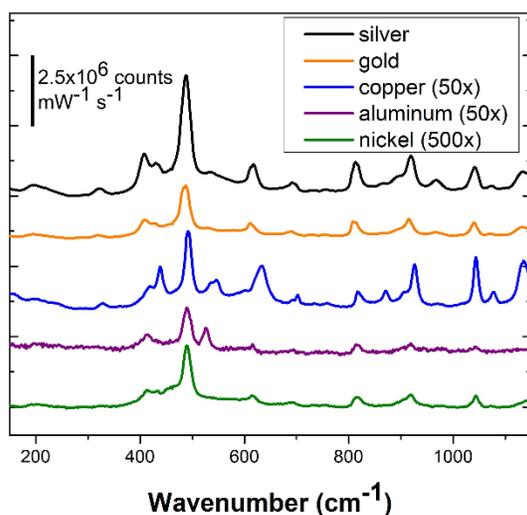
Figure 17. A comparison of SERS intensity observed for thionine adsorbed onto substrates of each of the five metals. Full monolayer coverage is assumed. Metals are presented in order of observed SERS intensity. Silver gives the more intense SERS as is expected based on theoretical calculations and experimental results from the literature. Here, silver gives 4.3×10^6 counts per milliwatt per second and is followed by gold.

C. Simulations for a Simple Model System

To better account for the near field contributions to the SERS enhancements (which should largely account for most of the measured enhancement variations among the five metals), numerical simulations were carried out using a simple system of two closely-spaced silica@metal core-shell particles. The particles had offset centers to mimic approximately the shapes of the elements in our nanogratings. Illuminated by a linearly polarized plane wave of unit magnitude, the scattered fields in the vicinity of the core-shell particles were simulated using the finite element package COMSOL Multiphysics V 5.2a (COMSOL, Stockholm, Se) and the Wave Optics add-on module, by solving the following governing equation:

$$\nabla \times (\nabla \times E) - k_0^2 \varepsilon_r E = 0 \qquad \text{(Eq. 19)}$$

in which E is the electric field vector, k_0, is the propagation constant. The relative permittivity is defined by

$$\varepsilon_r = (n - ik)^2 \qquad \text{(Eq. 20)}$$

where n and k are the real and imaginary components of the index of refraction.[83–85]

Equation 18 was discretized using quadratic complex elements and solved in the frequency domain. Perfectly Matched Layers (PMLs) are used to minimize numerical scattering at the boundaries of the computational domain. The geometric parameters are: pitch = 330 nm, d_{SiO2} = 270 nm, metal thickness = 22.5 nm, and gap = 15 nm. **Figure 18** shows the mesh used for the two particle simulations. In all cases the mesh is chosen so that the solution is independent of the mesh.
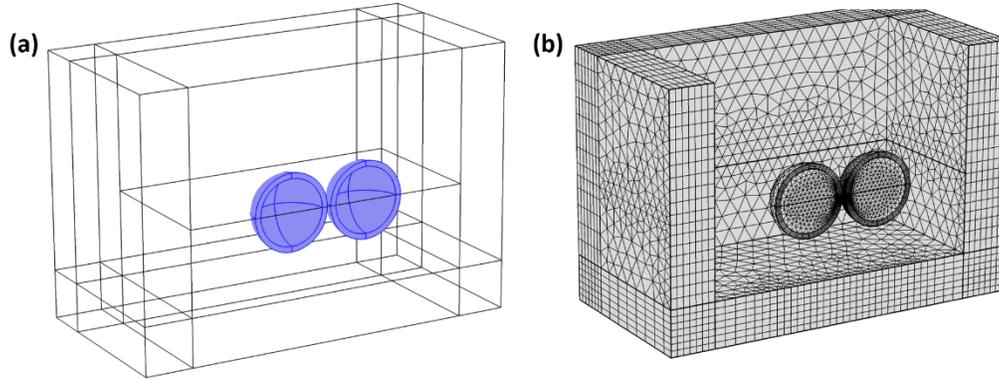
Figure 18. A system of two closely-spaced particles as illustrated in (a) was modeled, consisting of core-shell particles represented by a 270 nm diameter sphere of silica surrounded by a 315 nm diameter sphere of metal, whose centers were offset to represent the anisotropy of the structures. The spheres are separated by a gap of 15 nm. The mesh that is generated in COMSOL is shown in (b), including the Perfectly Matched Layers used to minimize numerical scattering at the boundaries. The depiction of the mesh is courtesy of Carl Meinhart, who also performed the numerical simulations.

The incident plane wave propagates in the negative z-direction, with a free space wavelength of $\lambda_0 = 632$ nm ($f_0 = 4.7436$ x 10^{14} Hz). Optical properties used in this simulation are listed in **Appendix 1**. The ambient medium was taken to be water to simulate Raman measurements in which the adsorbate is deposited onto the SERS substrate from solution. The maximum value of E^4 over the water domain was calculated, and the center plane showing $|E|^2$ for the various metals (normalized by a source with unity magnitude) are shown in **Figure 19**.

Figure 19. The center plane for the model is shown in (a) to elucidate what is follows in (b) – (f). The maximum value of E^4 over the water domain was calculated, and the center plane showing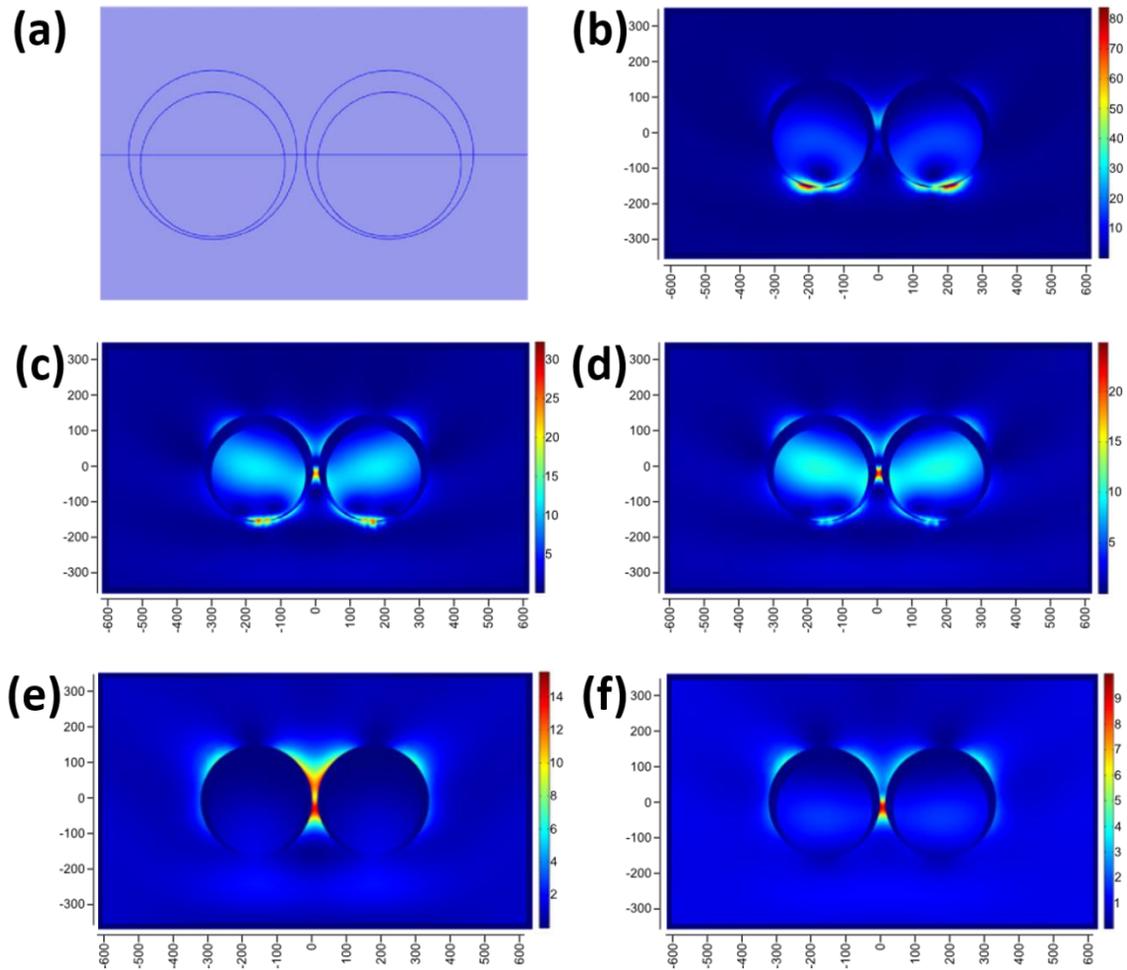 $|E|^2$ for silver (b), gold (c), copper (d), aluminum (e), and nickel (f) is shown (normalized by a source with unity magnitude).

The experimental and simulated intensities presented in **Figure 20** are, respectively, scaled to the experimental and simulated SERS intensities measured and calculated for the silver substrate. The agreement between the observed relative SERS enhancement magnitudes and metal to metal trends and the calculated values is quite good, suggesting that the major source of enhancement originates from the grating effect, which contributes approximately the same level of enhancement for each of the metals. This implies that it is the near field contribution that accounts for the major source of variation in the SERS enhancement among the five metals, reported in **Figure 20**.
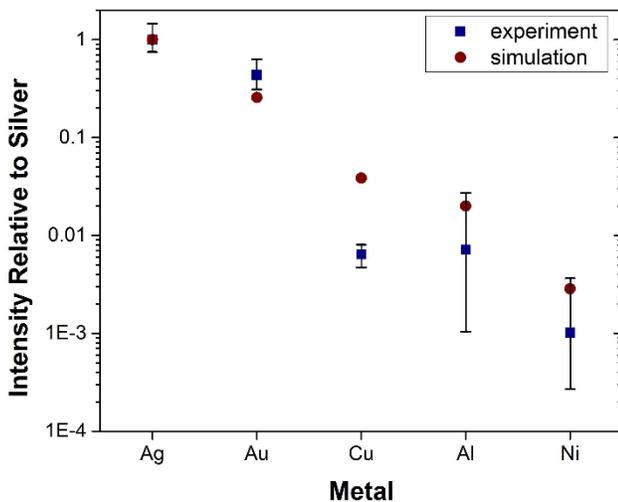
Figure 20. Relative experimental SERS intensities are compared to relative simulated intensities. All values are scaled to those of silver. Accordingly, the value of the relative enhancement for silver, the most enhancing metal of the five is unity and that for all other metals is less than unity. The simulated results show that the expected intensities span three orders of magnitude, which can be traced back to the dielectric functions of each metal. The experimental data trends with the simulated results, and while this means that the measured SERS intensities span three orders of magnitude, even the least enhancing metal, nickel, gives intensities on the order of 10^4 counts per milliwatt per second. Error bars represent the highest and lower intensities obtained across all substrates measured and the marker represents the average of all obtained intensities.

We have shown that even nickel, with poor plasmonic prospects on account of its moderate electrical conductivity and large interband contributions to its dielectric function, can be properly structure to achieve substantial SERS intensities using foundry-based, readily-scalable techniques; and this has implications for other poor plasmonic metals. Together with the other four metals our results suggest that by using a two-dimensional nanograting structure, essentially any material with sufficient electrical conductivity (including almost any metal and many alloys) can be used to create good SERS substrates which can produce large SERS signals when excited with low laser powers, and with a resonance in the visible region of the spectrum, that, moreover, can be tuned by suitably choosing the structural parameters of the grating; making it possible to use SERS as a more general tool than heretofore, for studying surface processes and catalysis in an operando mode.[86]

IV.   SERS Substrate Implementation

In this chapter, a broad overview will be given of exploration into applications for our SERS substrate architecture. For all applications discussed here, a standard silver-coated substrate is used, consisting of a grating with a 330 nm pitch onto which 200 nm of silica and 100 nm of silver are deposited with a 4 nm Ti adhesive layer between the silica and silver. A standard pre-treatment procedure was used to ensure the surface is cleared of any air-formed oxide and contaminants that may interfere with adsorption onto the metallic surfaces.

A. Solution-Phase Detection of Opioids

Recent years have seen an increase in the worldwide drug trade, posing a threat to both public health and national security. Heroin and other opioids comprises a substantial portion of this rise in illicit substances.[87,88] We chose to initially focus on detection of papaverine, an alkaloid unique to the latex of poppies.[89] Papaverine would act as prima facie evidence if found on the skin of individuals who have been handling large quantities of poppies

First, we sought to show that papaverine can in fact be identified using SERS, and so a range of concentrations was chosen (10^{-3}M down to 10^{-9}M) to represent 100s of parts per million down to less than 1 part per billion, which will encompass any forensically relevant concentration in bodily samples. Silver-coated substrates were selected for this particular application in part because the papaverine molecule has a relatively strong affinity for silver and because silver gives the strongest enhancements of all metals studied with this architecture. **Figure 21** shows the SERS spectra obtained for each concentration, and at all concentrations the spectrum is well-defined with good signal-to-noise, which can be obtained with low incident power and exposure time (7.6 µW, 2.5 seconds).
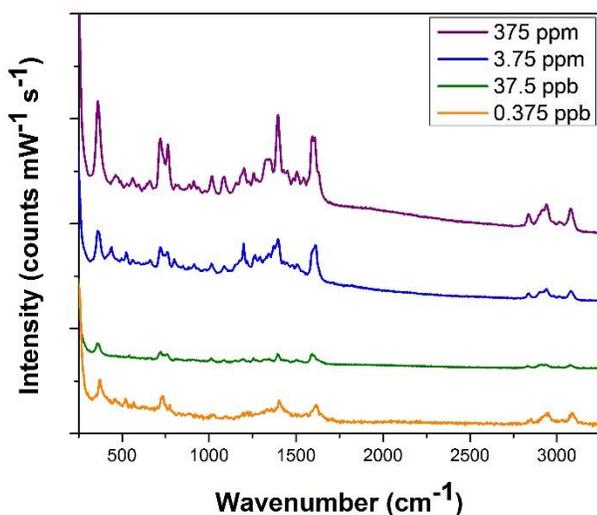
Figure 21. SERS spectrum for papaverine on silver from solutions with concentration ranging from 10^{-3}M (375 ppm) to 10^{-9}M (0.375 ppm). For all concentrations, the spectrum is well-defined with excellent signal-to-noise ratio, and is obtained using a low incident power and exposure time.

We next chose to test the feasibility of detecting other interesting opioids from solution using these substrates, so morphine and fentanyl were chosen. Rising opioid prescription rates and thus, opioid dependence in the United States presents a growing public health problem.[88] Additionally, fentanyl is a synthetic opioid that is one hundred times more potent than morphine and is a problematic cutting agent that is a notable cause of overdose.[90] Consequently, these is a demand for drug testing methods that is portable, rapid, readily implemented with minimal training, gives high specificity, and is sensitive in a biologically relevant range. SERS spectra for several opioids are already present in the literature using nanoparticle aggregates.[91]

Not unexpectedly, we can readily detect both morphine and fentanyl from solution using silver-coated substrates and rapid, low incident power conditions for spectrum collection

(7.6 µW, 2.5 seconds) and the result at the lowest concentration (10^{-9}M or <1 ppb) is presented in **Figure 22**.
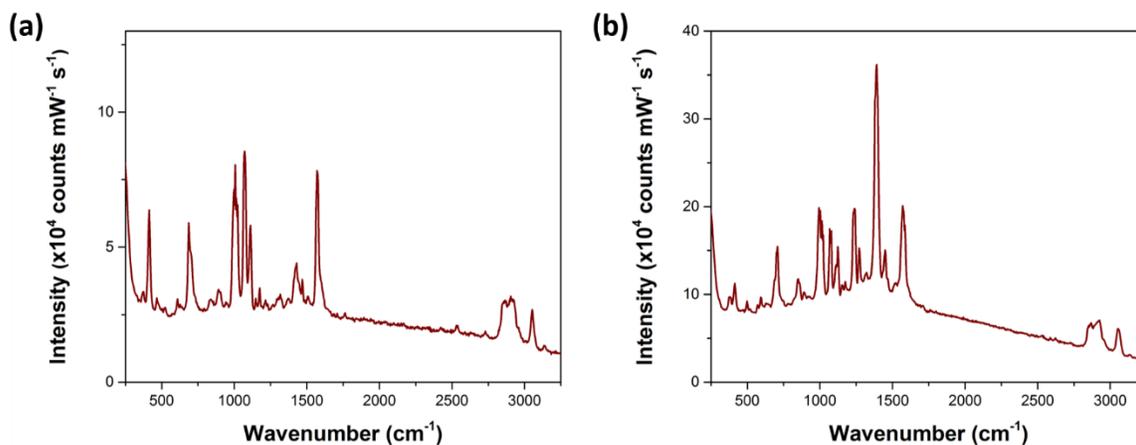
Figure 22. (a) SERS spectrum for fentanyl adsorbed on a silver substrate from a <1 ppb solution; (b) SERS spectrum for morphine adsorbed on a silver substrate from a <1 ppb solution; both spectra are well-defined and are collection using a low incident power and exposure time.

Solution phase SERS detection of papaverine, morphine, and fentanyl demonstrates that these analytes and applications targeting them are good candidates for analysis using our SERS substrates. The creation of a fieldable assay, however, requires a more carefully-designed detection system to address issues regarding the nature of the sample, sample handling, and whether meaningful concentration information can be determined from the SERS intensity.

B. *Exerting Microfluidic Control Over Sample Introduction*

Microfluidics was chosen as our method of sample handling, and combined SERS-microfluidics systems can be found in the literature.[92,93] This detection scheme is partially motivated by work done in collaboration with Army Research at the Edgewood Chemical Biological Center (ECBC) and Snowy Range Instruments (Wyoming), a manufacturer of

handheld Raman systems. An initial demonstration of SERS in a microfluidic channel done with silver colloids was done with papaverine and other drugs of interest.[89,94] Introduction of our SERS substrate architectures into that design in place of silver colloids would represent a significant advance in the ability to create a system that is truly fieldable by increasing the sensitivity and reliability of the detection and increasing the stability and ease of fabrication of the SERS portion.

The primary design goal was to create a microfluidic device consisting of a single channel in which our substrate architecture is incorporated as one of the walls of the channel. A conceptual illustration of the design and the fabrication scheme is shown in **Figure 23a**. In collaboration with Rustin Mirsafavi of the Meinhart group (Mechanical Engineering, UCSB), a device was fabricated starting from a framework made from polydimethylsiloxane (PDMS). A microfluidic mold was made from silicon and SU-8 photoresist, and then PDMS was poured onto the mold and cured. The resulting framework allows for a SERS substrate to be dropped in and a glass sealing layer to be bonded to the PDMS, forming a channel over the substrate surface through which analyte solutions can be flowed.

The first generation of these devices were tested by flowing micromolar solutions of BPE at a rate of 100 µL per minute. The resulting SERS spectra from several time points are plotted in **Figure 23b**, showing that the spectrum for BPE is observable with good signal-to-noise after only a few minutes of exposure and that the intensity tends to increase with time. The increase in intensity with time would indicate that a well-designed flow experiment could allow for the determination of concentration from SERS intensity. Intensity varies with the number of molecules adsorbed onto the surface, not concentration of the solution,

though the number of molecules can be related to the concentration via Langmuir adsorption isotherms. In future generations of this device, measurements will focus on the time evolution of the SERS intensity such that concentration information can be determined by comparison to the rate at which intensity increases and the value at which intensity plateaus for a set of calibration curves.
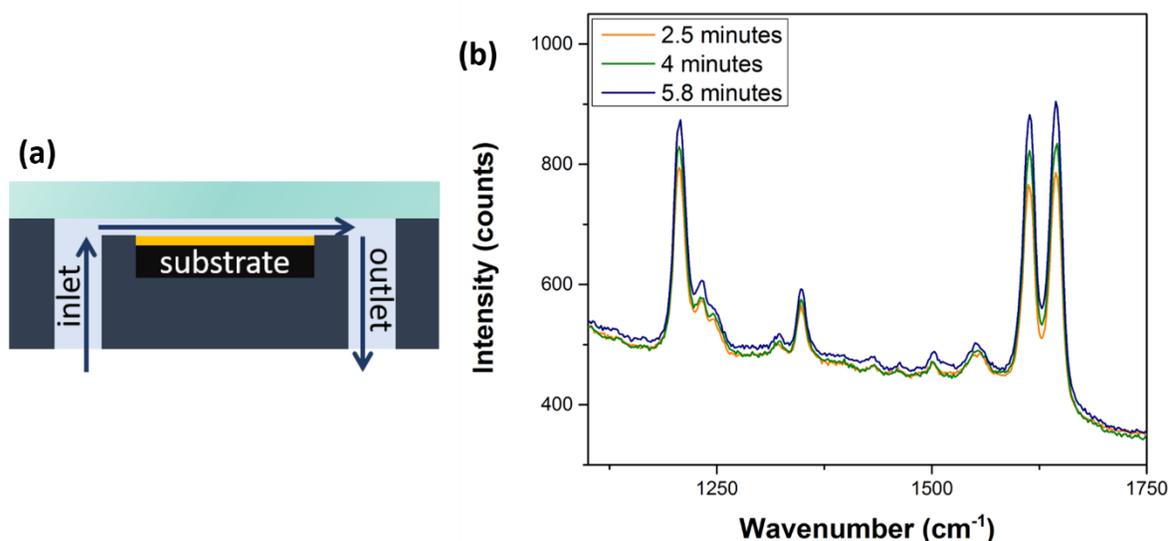
Figure 23. (a) schematic of a substrate incorporated into a microfluidic channel; (b) SERS spectra collected for BPE adsorbed on a silver substrate situated in a microfluidic channel at three time points after the initiation of flow at a rate of 100 µL per minute.

With these preliminary experiments, we have shown that microfluidics can be successfully combined with our SERS substrates and provide a more straightforward and reliable iteration of previous demonstrations of SERS in flow. Microfluidics provides greater control over the sample itself, allowing for more refined analysis of not only analyte identity but also analyte concentration. Our solid-state SERS architecture increases the reliability of SERS intensity information by virtue of its uniformity; in addition,

considerations of packaging and handling of the components of colloidal-based SERS systems typically used in flow are completely eliminated.

C. *Detection of Analytes from the Gas Phase*

A final avenue of exploration in this body of work focused on the implementation of our SERS substrates for the detection of gas phase, small molecule analytes. Certain small molecules may be of interest for breath analysis to detect small molecule biomarkers of certain diseases. One well known example is the presence of ketones bodies in the breath of an individual experiencing diabetic ketoacidosis (DKA). When the blood sugar of a diabetic individual becomes sufficiently low, the body exploits an alternative metabolic pathway— ketosis—in which acetyl CoA is converted into acetoacetate and β-hydroxybutyrate and the spontaneous breakdown product, acetone. Ketosis leads to the acidifying of the blood and other bodily tissues, a condition called acidosis and is often noted as a characteristically sweet smell on the breath of individuals experiencing DKA.[95]

A closed system was created containing a 5 x 5 mm silver-coated SERS substrate and small well of a given ketone. For demonstration purposes, acetone is shown in **Figure 25**, though a suite of ketones were tested, all with similar outcomes. Exposure of a substrate to the closed environment which is presumed to be saturated with acetone vapor gives rise to a SERS signal within a few minutes. Additionally, exposure of a substrate to 3-hydroxybutyric acid (a salt of β-hydroxybutyrate, dissolved in ethanol as a carrier vapor) resulted in a spectrum that gives peaks attributable to 3-hydroxybutyric acid.
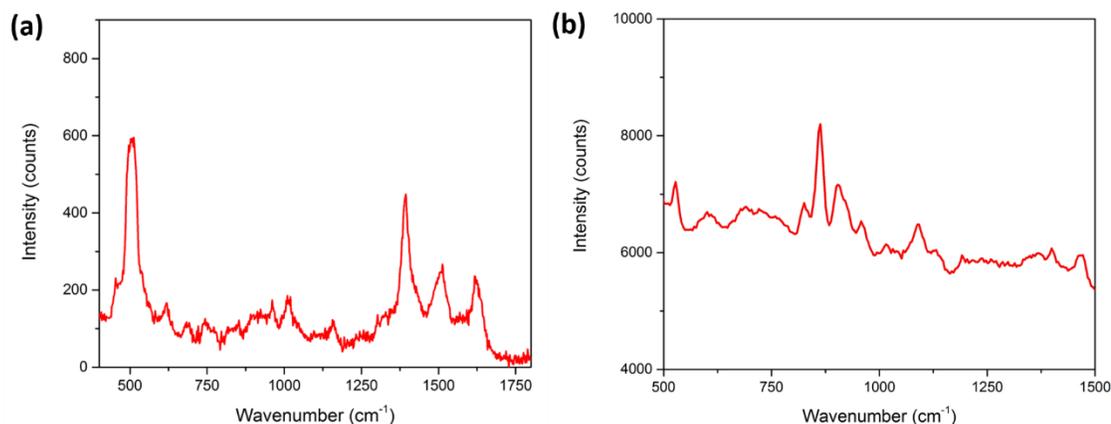
Figure 24. (a) SERS spectrum for acetone adsorbed onto a silver substrate from the gas phase of a closed environment in which the environment is saturated with acetone vapor. (b) SERS spectrum for 3-hydroxybutyric acid (3-OHB) adsorbed onto a silver substrate from the gas phase of a closed environment containing reservoir of 3-OHB dissolved in ethanol as a carrier vapor.

Ideally, a gas phase detection system would also exert some microfluidic-type control over the introduction of the sample to the substrate in order to minimize the needed volume of sample and to calibrate the concentration relative to the observed intensity. The above results are from experiments that need a higher level of sophistication before conclusions can be definitively drawn; however, the initial spectra inspire confidence in the feasibility of gas phase SERS detection of disease biomarkers.

V.   Conclusion

Since the discovery of SERS the development of ever more enhancing and reliable SERS substrates existed as a major goal in the field with incrementally more elegant, more controllable, more uniform and more enhancing nanostructures being reported. The work presented here builds on those efforts, producing a SERS substrate with among the highest reported enhancements, and certainly the highest reported degree of uniformity. We also

explicitly chose to use a fabrication scheme that employs readily scalable techniques from the silicon processing industry so facilitate the routine production of substrates in a large format. It yields enhancements on the order of 10^7 for gold-coated substrates. Although the system is specifically tuned to work with our 633 nm laser used for Raman excitation, the fabrication scheme has built in tunability to suit virtually any Raman excitation wavelength. Adjustment of a few geometric parameters including grating pitch and the size of the gap between neighboring grating elements are straightforward manipulations to bring about shifts in the relevant resonances. In addition to geometric parameters, we also showed that the system fabrication scheme is amenable to building SERS substrates using metals more chemically-interesting than gold or silver. We showed that depositing any material of sufficiently high electrical conductivity in place of gold will still result in a high-performing SERS system driven primarily by the first order grating resonance attributable to the architecture rather than the chosen material. The choice of material, as demonstrated both experimentally and in simulation, has influence only over relative performance by influence the near-field interactions between neighboring elements of the grating structure. This is a breakthrough in the SERS literature, which has relied heavily on silver and gold-based systems, opening up a wide range of new chemistries on catalytically interesting materials that can either be leveraged for analytical purposes or can themselves be studied in an operando mode.

As a demonstration of the power of this SERS system, we demonstrated the feasibility of schemes to detect analytes from the solution phase and the gas phase. In the solution phase, we were able to readily detect several opioids that have significance for both the forensic and public health communities. Introducing microfluidic control further enhances the

capabilities of this scheme, lending control over the sample volume in such a way that will allow for the determination of concentration instead of a simple positive/negative identification. A similar aspiration for gas phase detection has been outlined for the detection of small molecule biomarkers of disease in breath samples. Libraries of these small molecule biomarkers have been established in the medical literature, and a versatile SERS architecture such as ours has the potential to be instituted for breath analysis.

Ultimately, this work lays a foundation for high-performance, reliable SERS in any number of imaginable applications. SERS has the potential to combine the benefits of chemical specificity from vibrational spectroscopy with the high sensitivity made possible by surface enhancement effects. We have created a platform that gives the specificity and sensitivity in an effective manner, and hopefully, inspires the use of SERS in place of currently-used techniques that cannot offer the same.

References

1. Young, A. T. Rayleigh scattering. *Appl. Opt.* **20,** 533 (1981).

2. Manneback, C. Die Intensität und Polarisation der von zweiatomigen Molekülen gestreuten kohärenten und inkohärenten Strahlung. *Z. Für Phys.* **62,** 224–252 (1930).

3. Placzek, G. & Teller, E. Die Rotationsstruktur der Ramanbanden mehratomiger Moleküle. *Z. Für Phys.* **81,** 209–258 (1933).

4. Harris, D. C. & Bertolucci, M. D. *Symmetry and spectroscopy: an introduction to vibrational and electronic spectroscopy*. (Dover Publications, 1989).

5. Fleischmann, M., Hendra, P. J. & McQuillan, A. J. Raman spectra of pyridine adsorbed at a silver electrode. *Chem. Phys. Lett.* **26,** 163–166 (1974).

6. Jeanmaire, D. L. & Van Duyne, R. P. Surface raman spectroelectrochemistry. *J. Electroanal. Chem. Interfacial Electrochem.* **84,** 1–20 (1977).

7. Albrecht, M. G. & Creighton, J. A. Anomalously intense Raman spectra of pyridine at a silver electrode. *J. Am. Chem. Soc.* **99,** 5215–5217 (1977).

8. Moskovits, M. Surface roughness and the enhanced intensity of Raman scattering by molecules adsorbed on metals. *J. Chem. Phys.* **69,** 4159–4161 (1978).

9. Aravind, P. K., Nitzan, A. & Metiu, H. The interaction between electromagnetic resonances and its role in spectroscopic studies of molecules adsorbed on colloidal particles or metal spheres. *Surf. Sci.* **110,** 189–204 (1981).

10. Uppitsch, M. E. Observation of surface enhanced raman spectra by adsorption to silver colloids. *Chem. Phys. Lett.* **74,** 125–127 (1980).

11. Lee, P. C. & Meisel, D. Adsorption and surface-enhanced Raman of dyes on silver and gold sols. *J. Phys. Chem.* **86,** 3391–3395 (1982).

12. Moskovits, M. & Suh, J. S. Surface selection rules for surface-enhanced Raman spectroscopy: calculations and application to the surface-enhanced Raman spectrum of phthalazine on silver. *J. Phys. Chem.* **88,** 5526–5530 (1984).

13. Schatz, G. C. Theoretical studies of surface enhanced Raman scattering. *Acc. Chem. Res.* **17,** 370–376 (1984).

14. Vo-Dinh, T., Hiromoto, M. Y. K., Begun, G. M. & Moody, R. L. Surface-enhanced Raman spectrometry for trace organic analysis. *Anal. Chem.* **56,** 1667–1670 (1984).

15. Gao, P., Gosztola, D., Leung, L.-W. H. & Weaver, M. J. Surface-enhanced Raman scattering at gold electrodes: dependence on electrochemical pretreatment conditions and comparisons with silver. *J. Electroanal. Chem. Interfacial Electrochem.* **233,** 211–222 (1987).

16. Kneipp, K. *et al.* Single Molecule Detection Using Surface-Enhanced Raman Scattering (SERS). *Phys. Rev. Lett.* **78,** 1667–1670 (1997).

17. Emory, S. R., Haskins, W. E. & Nie, S. Direct Observation of Size-Dependent Optical Enhancement in Single Metal Nanoparticles. *J. Am. Chem. Soc.* **120,** 8009–8010 (1998).

18. Moskovits, M. Surface-enhanced spectroscopy. *Rev. Mod. Phys.* **57,** 783–826 (1985).

19. *Surface-enhanced raman scattering: physics and applications*. (Springer, 2006).

20. Mulvaney, P. Surface Plasmon Spectroscopy of Nanosized Metal Particles. *Langmuir* **12,** 788–800 (1996).

21. Jackson, J. D. *Classical electrodynamics*. (Wiley, 1999).

22. Gersten, J. & Nitzan, A. Electromagnetic theory of enhanced Raman scattering by molecules adsorbed on rough surfaces. *J. Chem. Phys.* **73,** 3023–3037 (1980).

23.   McCall, S. L., Platzman, P. M. & Wolff, P. A. Surface enhanced Raman scattering. *Phys. Lett. A* **77,** 381–383 (1980).

24.   Wang, D.-S., Chew, H. & Kerker, M. Enhanced Raman scattering at the surface (SERS) of a spherical particle. *Appl. Opt.* **19,** 2256 (1980).

25.   Xu, H. & Käll, M. Polarization-Dependent Surface-Enhanced Raman Spectroscopy of Isolated Silver Nanoaggregates. *ChemPhysChem* **4,** 1001–1005 (2003).

26.   Creighton, J. A. The effective Raman tensor for SER scattering by molecules adsorbed at the surface of a spherical particle. *Surf. Sci.* **158,** 211–221 (1985).

27.   Maier, S. A. *Plasmonics: fundamentals and applications*. (Springer, 2007).

28.   Kittel, C. *Introduction to solid state physics*. (Wiley, 2005).

29.   Aravind, P. K. & Metiu, H. Use of a perfectly conducting sphere to excite the plasmon of a flat surface. 1. Calculation of the local field with applications to surface-enhanced spectroscopy. *J. Phys. Chem.* **86,** 5076–5084 (1982).

30.   Gersten, J. & Nitzan, A. Spectroscopic properties of molecules interacting with small dielectric particles. *J. Chem. Phys.* **75,** 1139–1152 (1981).

31.   Porter, M. D., Lipert, R. J., Siperko, L. M., Wang, G. & Narayanan, R. SERS as a Bioassay Platform: Fundamentals, Design, and Applications. *Chem Soc Rev* **37,** 1001–1011 (2008).

32.   Sylvia, J. M., Janni, J. A., Klein, J. D. & Spencer, K. M. Surface-Enhanced Raman Detection of 2,4-Dinitrotoluene Impurity Vapor as a Marker to Locate Landmines. *Anal Chem* **72,** 5834–5840 (2000).

33.   Brosseau, C. L., Casadio, F. & Van Duyne, R. P. Revealing the Invisible: Using Surface-Enhanced Raman Spectroscopy to Identify Minute Remnants of Color in Winslow Homer's Colorless Skies. *J Raman Spectrosc* **42,** 1305–1310 (2011).

34.   Yan, F. & Vodinh, T. Surface-enhanced Raman scattering detection of chemical and biological agents using a portable Raman integrated tunable sensor. *Sens. Actuators B Chem.* **121,** 61–66 (2007).

35.   Banholzer, M. J., Millstone, J. E., Qin, L. & Mirkin, C. A. Rationally designed nanostructures for surface-enhanced Raman spectroscopy. *Chem. Soc. Rev.* **37,** 885 (2008).

36.   Kneipp, K., Kneipp, H., Itzkan, I., Dasari, R. R. & Feld, M. S. Ultrasensitive Chemical Analysis by Raman Spectroscopy. *Chem. Rev.* **99,** 2957–2976 (1999).

37.   Toderas, F., Baia, M., Baia, L. & Astilean, S. Controlling gold nanoparticle assemblies for efficient surface-enhanced Raman scattering and localized surface plasmon resonance sensors. *Nanotechnology* **18,** 255702 (2007).

38.   Jiao, Y., Ryckman, J. D., Koktysh, D. S. & Weiss, S. M. Controlling surface enhanced Raman scattering using grating-type patterned nanoporous gold substrates. *Opt. Mater. Express* **3,** 1137 (2013).

39.   Dickey, M. D. *et al.* Fabrication of Arrays of Metal and Metal Oxide Nanotubes by Shadow Evaporation. *ACS Nano* **2,** 800–808 (2008).

40.   Driskell, J. D. *et al.* The Use of Aligned Silver Nanorod Arrays Prepared by Oblique Angle Deposition as Surface Enhanced Raman Scattering Substrates. *J. Phys. Chem. C* **112,** 895–901 (2008).

41.   Haynes, C. L. & Van Duyne, R. P. Nanosphere Lithography: A Versatile Nanofabrication Tool for Studies of Size-Dependent Nanoparticle Optics. *J. Phys. Chem. B* **105,** 5599–5611 (2001).

42.   Yan, B. *et al.* Engineered SERS Substrates with Multiscale Signal Enhancement: Nanoparticle Cluster Arrays. *ACS Nano* **3,** 1190–1202 (2009).

43.   Meier, M., Liao, P. F. & Wokaun, A. Enhanced fields on rough surfaces: dipolar interactions among particles of sizes exceeding the Rayleigh limit. *J. Opt. Soc. Am. B* **2,** 931 (1985).

44.   Lamprecht, B. *et al.* Metal Nanoparticle Gratings: Influence of Dipolar Particle Interaction on the Plasmon Resonance. *Phys. Rev. Lett.* **84,** 4721–4724 (2000).

45.   Chu, Y., Schonbrun, E., Yang, T. & Crozier, K. B. Experimental observation of narrow surface plasmon resonances in gold nanoparticle arrays. *Appl. Phys. Lett.* **93,** 181108 (2008).

46.   García-Vidal, F. J. & Pendry, J. B. Collective Theory for Surface Enhanced Raman Scattering. *Phys. Rev. Lett.* **77,** 1163–1166 (1996).

47.   Kocabas, A., Ertas, G., Senlik, S. S. & Aydinli, A. Plasmonic band gap structures for surface-enhanced Raman scattering. *Opt. Express* **16,** 12469 (2008).

48.   Curtin, B. M., Fang, E. W. & Bowers, J. E. Highly Ordered Vertical Silicon Nanowire Array Composite Thin Films for Thermoelectric Devices. *J. Electron. Mater.* **41,** 887–894 (2012).

49.   Hutchinson, K., Hester, R. E., Albery, W. J. & Hillman, A. R. Raman spectroscopic studies of a thionine-modified electrode. *J. Chem. Soc. Faraday Trans. 1 Phys. Chem. Condens. Phases* **80,** 2053 (1984).

50.   Le Ru, E. C., Blackie, E., Meyer, M. & Etchegoin, P. G. Surface Enhanced Raman Scattering Enhancement Factors: A Comprehensive Study. *J. Phys. Chem. C* **111,** 13794–13803 (2007).

51.   Dignam, M. J., Moskovits, M. & Stobie, R. W. Specular reflectance and ellipsometric spectroscopy of oriented molecular layers. *Trans. Faraday Soc.* **67,** 3306 (1971).

52.   Azzam, R. M. A.-G. & Bashara, N. M. *Ellipsometry and polarized light*. (Elsevier, 1999).

53.   Long, D. A. *The Raman effect: a unified treatment of the theory of Raman scattering by molecules*. (Wiley, 2002).

54.	Zuloaga, J., Prodan, E. & Nordlander, P. Quantum Plasmonics: Optical Properties and Tunability of Metallic Nanorods. *ACS Nano* **4,** 5269–5276 (2010).

55.	Liver, N., Nitzan, A. & Gersten, J. I. Local fields in cavity sites of rough dielectric surfaces. *Chem. Phys. Lett.* **111,** 449–454 (1984).

56.	Fang, Y., Seong, N.-H. & Dlott, D. D. Measurement of the Distribution of Site Enhancements in Surface-Enhanced Raman Scattering. *Science* **321,** 388–392 (2008).

57.	Laurence, T. A., Braun, G. B., Reich, N. O. & Moskovits, M. Robust SERS Enhancement Factor Statistics Using Rotational Correlation Spectroscopy. *Nano Lett.* **12,** 2912–2917 (2012).

58.	Wu, Q. *et al.* Short pitch metal gratings and methods for making the same. (2013).

59.	David, C., Guillot, N., Shen, H., Toury, T. & Chapelle, M. L. de la. SERS detection of biomolecules using lithographed nanoparticles towards a reproducible SERS biosensor. *Nanotechnology* **21,** 475501 (2010).

60.	Graham, D. & Goodacre, R. Chemical and bioanalytical applications of surface enhanced Raman scattering spectroscopy. *Chem. Soc. Rev.* **37,** 883 (2008).

61.	Wustholz, K. L., Brosseau, C. L., Casadio, F. & Van Duyne, R. P. Surface-enhanced Raman spectroscopy of dyes: from single molecules to the artists' canvas. *Phys. Chem. Chem. Phys.* **11,** 7350 (2009).

62.	Willets, K. A. & Van Duyne, R. P. Localized Surface Plasmon Resonance Spectroscopy and Sensing. *Annu. Rev. Phys. Chem.* **58,** 267–297 (2007).

63.	Kelly, K. L., Coronado, E., Zhao, L. L. & Schatz, G. C. The Optical Properties of Metal Nanoparticles: The Influence of Size, Shape, and Dielectric Environment. *J. Phys. Chem. B* **107,** 668–677 (2003).

64.	West, P. R. *et al.* Searching for better plasmonic materials. *Laser Photonics Rev.* **4,** 795–808 (2010).

65.   Pettinger, B., Picardi, G., Schuster, R. & Ertl, G. Surface-enhanced and STM-tip-enhanced Raman Spectroscopy at Metal Surfaces. *Single Mol.* **3,** 285–294 (2002).

66.   Moskovits, M. Surface-enhanced Raman spectroscopy: a brief retrospective. *J. Raman Spectrosc.* **36,** 485–496 (2005).

67.   Zeman, E. J. & Schatz, G. C. An accurate electromagnetic theory study of surface enhancement factors for silver, gold, copper, lithium, sodium, aluminum, gallium, indium, zinc, and cadmium. *J. Phys. Chem.* **91,** 634–643 (1987).

68.   Kolwas, K., Demianiuk, S. & Kolwas, M. Plasmon resonances observed in light scattered by large alkali clusters. *Appl. Phys. B Lasers Opt.* **65,** 63–68 (1997).

69.   Chan, G. H., Zhao, J., Hicks, E. M., Schatz, G. C. & Van Duyne, R. P. Plasmonic Properties of Copper Nanoparticles Fabricated by Nanosphere Lithography. *Nano Lett.* **7,** 1947–1952 (2007).

70.   Abdelsalam, M. E., Mahajan, S., Bartlett, P. N., Baumberg, J. J. & Russell, A. E. SERS at Structured Palladium and Platinum Surfaces. *J. Am. Chem. Soc.* **129,** 7399–7406 (2007).

71.   Langhammer, C., Yuan, Z., Zorić, I. & Kasemo, B. Plasmonic Properties of Supported Pt and Pd Nanostructures. *Nano Lett.* **6,** 833–838 (2006).

72.   Knight, M. W. *et al.* Aluminum for Plasmonics. *ACS Nano* **8,** 834–840 (2014).

73.   Chen, J. *et al.* Plasmonic Nickel Nanoantennas. *Small* **7,** 2341–2347 (2011).

74.   Kumamoto, Y. *et al.* Indium for Deep-Ultraviolet Surface-Enhanced Resonance Raman Scattering. *ACS Photonics* **1,** 598–603 (2014).

75.   Ross, M. B. & Schatz, G. C. Aluminum and Indium Plasmonic Nanoantennas in the Ultraviolet. *J. Phys. Chem. C* **118,** 12506–12514 (2014).

76. Zhao, L., Kelly, K. L. & Schatz, G. C. The Extinction Spectra of Silver Nanoparticle Arrays: Influence of Array Structure on Plasmon Resonance Wavelength and Width [†]. *J. Phys. Chem. B* **107,** 7343–7350 (2003).

77. Wu, B. *et al.* Plasmon-Mediated Photocatalytic Decomposition of Formic Acid on Palladium Nanostructures. *Adv. Opt. Mater.* **4,** 1041–1046 (2016).

78. Kanipe, K. N., Chidester, P. P. F., Stucky, G. D. & Moskovits, M. Large Format Surface-Enhanced Raman Spectroscopy Substrate Optimized for Enhancement and Uniformity. *ACS Nano* **10,** 7566–7571 (2016).

79. Leung, L. W. H. & Weaver, M. J. Extending surface-enhanced raman spectroscopy to transition-metal surfaces: carbon monoxide adsorption and electrooxidation on platinum- and palladium-coated gold electrodes. *J. Am. Chem. Soc.* **109,** 5113–5119 (1987).

80. Shiju, N. R. & Guliants, V. V. Recent developments in catalysis using nanostructured materials. *Appl. Catal. Gen.* **356,** 1–17 (2009).

81. Aiken, J. D. & Finke, R. G. A review of modern transition-metal nanoclusters: their synthesis, characterization, and applications in catalysis. *J. Mol. Catal. Chem.* **145,** 1–44 (1999).

82. Roucoux, A., Schulz, J. & Patin, H. Reduced Transition Metal Colloids: A Novel Family of Reusable Catalysts? *Chem. Rev.* **102,** 3757–3778 (2002).

83. Johnson, P. B. & Christy, R. W. Optical Constants of the Noble Metals. *Phys. Rev. B* **6,** 4370–4379 (1972).

84. Rakić, A. D., Djurišić, A. B., Elazar, J. M. & Majewski, M. L. Optical properties of metallic films for vertical-cavity optoelectronic devices. *Appl. Opt.* **37,** 5271 (1998).

85. Johnson, P. & Christy, R. Optical constants of transition metals: Ti, V, Cr, Mn, Fe, Co, Ni, and Pd. *Phys. Rev. B* **9,** 5056–5070 (1974).

86.   Bañares, M. A. Operando methodology: combination of in situ spectroscopy and simultaneous activity measurements under catalytic reaction conditions. *Catal. Today* **100,** 71–77 (2005).

87.   United Nations. *World drug report 2015.* (United Nations Pubns, 2015).

88.   Degenhardt, L. *et al.* The global epidemiology and burden of opioid dependence: results from the global burden of disease 2010 study: Epidemiology and burden of opioid dependence. *Addiction* **109,** 1320–1333 (2014).

89.   Mirsafavi, R. Y. *et al.* Detection of Papaverine for the Possible Identification of Illicit Opium Cultivation. *Anal. Chem.* **89,** 1684–1688 (2017).

90.   Kuhlman, J. J., McCaulley, R., Valouch, T. J. & Behonick, G. S. Fentanyl Use, Misuse, and Abuse: A Summary of 23 Postmortem Cases. *J. Anal. Toxicol.* **27,** 499–504 (2003).

91.   Rana, V., Cañamares, M. V., Kubic, T., Leona, M. & Lombardi, J. R. Surface-enhanced Raman Spectroscopy for Trace Identification of Controlled Substances: Morphine, Codeine, and Hydrocodone: Surface-enhanced Raman spectroscopy for trace identification. *J. Forensic Sci.* **56,** 200–207 (2011).

92.   Andreou, C., Hoonejani, M. R., Barmi, M. R., Moskovits, M. & Meinhart, C. D. Rapid Detection of Drugs of Abuse in Saliva Using Surface Enhanced Raman Spectroscopy and Microfluidics. *ACS Nano* **7,** 7157–7164 (2013).

93.   Pallaoro, A., Hoonejani, M. R., Braun, G. B., Meinhart, C. D. & Moskovits, M. Rapid Identification by Surface-Enhanced Raman Spectroscopy of Cancer Cells at Low Concentrations Flowing in a Microfluidic Channel. *ACS Nano* **9,** 4328–4336 (2015).

94.   Kline, N. D. *et al.* Optimization of Surface-Enhanced Raman Spectroscopy Conditions for Implementation into a Microfluidic Device for Drug Detection. *Anal. Chem.* **88,** 10513–10522 (2016).

95.   Chiasson, J.-L. *et al.* Diagnosis and treatment of diabetic ketoacidosis and the hyperglycemic hyperosmolar state. *CMAJ Can. Med. Assoc. J. J. Assoc. Medicale Can.* **168,** 859–866 (2003).

Appendix

Appendix 1. Table of Optical Constants Used for Numerical Simulations

	n	k
Water	1.330	0
SiO$_2$	1.4762	0
Ag[83]	0.057896	4.2718
Au[83]	0.17893	3.4305
Cu[83]	0.25736	3.4081
Al[84]	1.2629	7.2720
Ni[85]	1.9900	4.1081